NOVA SCHOOL OF SCIENCE & TECHNOLOGY

DEPARTMENT OF MATERIALS SCIENCE

ANA BEATRIZ TORCATO MARQUES

BSc in Micro and Nanotechnologies Engineering

Green Synthesis of Mg-TiO_2 Nanoparticles for Periodontal Tissue Engineering

MASTER IN MICRO AND NANOTECNHOLOGIES ENGINEERING

NOVA University Lisbon

October, 2025

NOVA SCHOOL OF SCIENCE & TECHNOLOGY

DEPARTMENT OF MATERIALS SCIENCE

Green Synthesis of Mg-TiO_2 Nanoparticles for Periodontal Tissue Engineering

ANA BEATRIZ TORCATO MARQUES

BSc in Micro and Nanotechnologies Engineering

Adviser: Dr. Daniela Nunes Gomes
Assistant Professor, NOVA School of Science and Technology, NOVA University Lisbon

Co-advisers: Dr. Henrique Vazão de Almeida
Assistant Researcher at CENIMAT|i3N, NOVA School of Science and Technology, NOVA University Lisbon

Examination Committee:

Chair: Name of the committee chairperson,
Full Professor, FCT-NOVA

Rapporteurs: Name of a rapporteur,
Associate Professor, Another University
Name of another rapporteur,
Assistant Professor, Another University

Adviser: Dr. Daniela Nunes Gomes,
Assistant Professor, NOVA School of Science and Technology

Members: Dr. Henrique Vazão de Almeida,
Assistant Researcher at CENIMAT|i3N, NOVA School of Science and Technology

MASTER IN MICRO AND NANOTECHNOLOGIES ENGINEERING

NOVA University Lisbon
October, 2025

Green Synthesis of Mg-TiO_2 Nanoparticles for Periodontal Tissue Engineering

Para a minha família.

ACKNOWLEDGMENTS

Firstly, I would like to thank the Department of Materials Science at NOVA School of Science and Technology and therefore thank all the professors that had an important role in my 5-year education. I would like to thank CENIMAT for providing the facilities and materials for the development of my thesis.

When you have only six months to make some of the most important decisions of your academic journey, it is crucial not to feel like you are doing it alone. Therefore, I would like to express my deepest gratitude to my adviser, Dr.ª Daniela Gomes, who always gave me guidance and helped me to achieve the best possible results. Thank you for your patience, time and knowledge, for always being available to answer my questions. Your thoughtful advice made it possible for my ideas to come to life.

To my co-adviser, Dr. Henrique Vazão de Almeida, thank you for your brilliant new ideas, without it, it would be impossible to move forward. Thank you for your constant support and positivity that helped me get through every part of my project.

I would like to also thank Dr.ª Leonor and future Dr.ª Maria, for all the help, guidance and support. To Dr.ª Leonor Matias, thank you for all the knowledge you passed to me, for all the availability, your guidance made me feel secure that I knew what I was doing. Thank you for always being there to listen to my questions. For Maria, thank you for always finding solutions when I thought that everything was doomed, thank you for your patience.

To my lovely friends Gerson and Beatriz, I would like to thank you for every moment we spent together at CENIMAT. Even when I was feeling down, you guys helped me to smile. To Gerson, thank you for being my "teacher", my confident, and the person I'm going to all concerts with. To Beatriz, thank you for being the sweetest soul I've met, your hugs were the best part of my day. I will cherish you forever.

To my lab partner João, thank you for sharing this experience with me. Every time something went wrong you always found a way to make it funny somehow (and a lot of things went wrong). In these last months I noticed how smart and dedicated you are, I'm sure you'll be extremely successful in what you choose to do. Nonetheless, I hope you don't forget about our days in CENIMAT. You got a friend in me.

To my best friend Ana, thank you for sharing the last few years with me, which has helped me through everything in my life. Thank you for always loving me, supporting me, and being there for me no matter what. I'm sure you'll be the most successful psychologist in the world. It's a blessing to have you in my life.

To Amélia, or my Melinha as I love to call you, thank you for being the person that is my second home. Thank you for understanding me and for being the most fun person to be around. I want to go everywhere in the world with you, build every memory by your side. I'm grateful for your existence in my life every single day.

To my friends Sofia, Bianca, Inês, David and Duarte I owe you a lot for the past years (some of you I owe you my entire life). Thank you for always listening to me and to push me to be the best version of myself every day.

To my family: to my mom and to my dad, thank you for always supporting me and for never doubting me. To my mom, you are the example of perseverance, which I can proudly say I inherited (that and almost everything I am today). To my dad, thank you for always caring not only for the last 6 months but specially throughout the last 5 years of my life. To my sister, thank you for being my role-model, you're everything I want to be and more, you inspire me every day. To my brother, thank you for always supporting me even if you don't say it, I can feel it (it's a twin's thing). To my grandma, thank you for making me food every weekend so I could have time to study more, thank you for believing in my capacities always.

To everyone, my genuine and most heartfelt thank you.

“To the edge of the universe and back. Endure and survive”
(The Last of Us Universe)

ABSTRACT

Nanotechnology has been essential for the resolution of diverse problems in medicine, bone tissue regeneration being one of them. The periodontal tissues can be compromised by chronic diseases such as periodontitis, a bacterial infection that leads to an immune response of the body that then causes bone resorption, therefore, tooth loss. Tissue engineering (TE) aims to develop innovative strategies to overcome the limitations of conventional therapies.

In this study, we report the synthesis of titanium dioxide (TiO_2) nanoparticles (NPs) with the incorporation of magnesium (Mg) in different concentrations (5, 7 and 10 mol. %) to enhance biocompatibility and mechanical performance. The NPs were produced via a microwave-assisted hydrothermal process without any extra treatment, resulting in a more sustainable and cost-effective approach. The anatase phase of the Mg-TiO_2 NPs was confirmed by X-ray diffraction (XRD) and Raman spectroscopy. Ultraviolet-Visible (UV-Vis) spectroscopy was performed to estimate the bandgap (Eg). Scanning transmission electron microscopy (STEM) revealed that 10 mol. % Mg-TiO_2 induced a morphological transformation into nanorods with structural surface defects. This sample exhibited uniform pore distribution and increased specific surface area (256.93 m^2g^{-1}).

The 10 mol. % Mg-TiO_2 NPs were incorporated into alginate scaffolds using blending and coating approaches. The resulting scaffolds demonstrated that coating led to a reduction in scaffold porosity while NPs incorporation also decreased water uptake. The incorporation of NPs resulted in only a slight, not statistically significant, increase in mechanical strength. Live/dead assays indicated that 10 mol. % Mg-TiO_2 NPs did not induce any cytotoxic effects on Saos-2 cells (cell viability above the 70 % threshold) proving their biocompatibility.

This study introduced a sustainable method for Mg-TiO_2 nanomaterials synthesis and highlights the potential of their incorporation into alginate scaffolds to improve osteoinductive and mechanical properties, overcoming issues in periodontal TE.

Keywords: periodontal tissues, tissue engineering, titanium dioxide, magnesium, biocompatibility, osteoinductive properties.

RESUMO

A nanotecnologia tem sido essencial na resolução de diversos problemas na medicina, sendo a regeneração dos tecidos ósseos um dos principais. Os tecidos periodontais podem ser comprometidos por doenças crónicas, como a periodontite, uma infeção bacteriana que desencadeia uma resposta imunitária, levando à reabsorção óssea e, consequentemente, à perda dentária. A engenharia de tecidos (TE) procura desenvolver estratégias inovadoras que superem as limitações das terapias convencionais.

Neste estudo, é reportada a síntese de nanopartículas (NPs) de dióxido de titânio (TiO_2) incorporadas com magnésio (Mg) em diferentes concentrações (5, 7 e 10 mol. %) para melhorar a biocompatibilidade e o desempenho mecânico. As NPs foram produzidas através de um processo hidrotérmico assistido por microondas, sem tratamento adicional, resultando numa abordagem mais sustentável e económica. A fase anatase das NPs de Mg-TiO_2 foi confirmada por difração de raios-X (XRD) e espectroscopia Raman. A espectroscopia Ultravioleta-Visível (UV-Vis) foi utilizada para estimar a energia de hiato (Eg). A microscopia eletrónica de transmissão de varrimento (STEM) mostrou que as NPs 10 mol. % de Mg-TiO_2 induziram uma transformação morfológica em *nanorods* com defeitos superficiais. Esta amostra apresentou distribuição de poros uniforme e aumento da área superficial específica (256.93 m^2g^{-1}).

As NPs de 10 mol. % Mg-TiO_2 foram incorporadas em *scaffolds* de alginato por mistura e encharcamento. Os resultados demonstraram que o encharcamento reduziu a porosidade e a incorporação das NPs diminuiu a absorção de água. Observou-se apenas um ligeiro aumento, não estatisticamente significativo, na resistência mecânica. Ensaios de viabilidade celular (Live/Dead) confirmaram a ausência de citotoxicidade em células Saos-2 (viabilidade > 70 %), comprovando a biocompatibilidade das NPs.

Este estudo apresenta um método sustentável para a síntese de nanomateriais de Mg-TiO_2 e evidencia o seu potencial na melhoria das propriedades osteoindutivas e mecânicas de *scaffolds* de alginato aplicados à TE periodontal.

Palavras chave: tecidos periodontais, engenharia de tecidos, dióxido de titânio, magnésio, biocompatibilidade, propriedades osteoindutivas.

CONTENTS

LIST OF FIGURES

LIST OF TABLES

ACRONYMS

3D	Three-Dimensional
Arb.	Arbitrary
BET	Brunauer-Emmett-Teller
BHJ	Barrett-Joyner-Halenda
ECM	Extracellular Matrix
EDAC	1-Ethyl-3-Dimethyl Aminopropyl Carbodiime
EDS	Energy-Dispersive X-ray Spectrometer
FEG	Field-Emission Gun
FFT	Fast Fourier Transform
FWHM	Full Width at Half Maximum
HAADF	High-Angle Annular Dark-Field
ICDD	International Centre for Diffraction Data
IPA	Isopropyl Alcohol
ISO	International Standard Organization
IUPAC	International Union of Pure and Applied Chemistry
NHS	N-Hydroxy-Succinimide

NPs	Nanoparticles
PBS	Phosphate-Buffered Saline
PI	Propidium Iodide
RT	Room Temperature
SD	Standard Deviation
SEM	Scanning Electron Microscopy
STEM	Scanning Transmission Electron Microscopy
TE	Tissue Engineering
TiO_2	Titanium Dioxide
UV-Vis-NIR	Ultraviolet-Visible-Near Infrared
XRD	X-Ray Diffraction

SYMBOLS

2θ	Angle between the incident and the diffracted beam
θ	Bragg angle (diffraction angle at which the peak is observed)
ºC	Degree Celsius
Δ	Variation in size
A	Proportionality constant
α	Absorption coefficient
β	Line broadening at half maximum intensity
θ	Bragg angle
E	Young's Modulus
σ	Stress
ε	Strain
Eg	Bandgap
hν	Photon energy
K	Scherrer Constant
m	Exponent that defines the nature of the electronic transition
mol. %	Molar percentage
n	Replicates
P/P_0	Relative pressure
P	Porosity

ρ	Density
τ	Average crystallite size
w	Mass
λ	Wavelength

1

INTRODUCTION

1.1 Periodontal Composition and Tissue Engineering

Clinical periodontics have been facing challenges in managing periodontal defects since the periodontium has several unique tissues that can be compromised in their own way. The periodontium involves hard and soft tissue, such as the periodontal ligament (PL), alveolar bone (AB) and cementum (CM) (**Figure 1**), therefore, the regeneration and reconstruction of the periodontium cannot be a simple one-trick solution but a three-dimensional (3D) repair [1-4].

Periodontitis is an infectious disease caused by pathogenic microorganisms in the subgingival biofilm, in combination with other risk factors, such as aging and smoking [5]. Untreated periodontitis results in irreversible destruction of the tooth-supporting tissues, including the PL, AB and CM, and may lead to early tooth loss (**Figure 1**) [5-6]. It has also been linked to systemic disorders, such as diabetes, rheumatoid arthritis, neurodegenerative disorders, and cardiovascular complications, and has been associated with adverse pregnancy outcomes [5]. Therefore, periodontal health may significantly impact a patient's quality of life [7-8].

Conventional treatment strategies were able to mechanically resolve more simple problems like removing the bacteria that is causing the disease, however it failed in regenerating the damaged tissues [5-6]. There comes the role of tissue engineering (TE), offering the opportunity to improve periodontal regeneration in a more predictable and qualitative but possibly less invasive manner. Restoring the tissue function through the delivery of stem cells, bioactive molecules, or synthetic tissue scaffolds engineered in the laboratory is the main goal of TE [2]. This field integrates distinct areas like materials science, genetics, biology, mechanical engineering, and clinical medicine, converging the knowledge from them all. It takes as a requirement the use of porous 3D scaffolds to provide appropriate micro-environment for regeneration, they act as a template for the formation of the new tissue [6-10].

Scaffolds play a central role in TE and therefore must be carefully designed. First, they must be biocompatible, enabling cells to adhere, migrate, proliferate, and maintain normal function without eliciting adverse host responses. After the implantation, the construct should trigger only minimal immune activity to avoid inflammation, scaffold degradation, or rejection [11]. Second, scaffolds should be biodegradable, gradually degrading as the newly formed tissue develops its own extracellular matrix (ECM). Importantly, the by-products must be non-toxic and capable of being metabolized or exit the body without interfering with other organs. Third, scaffolds require appropriate mechanical properties,

consistent to the anatomical site of implantation. They must have sufficient strength for surgical manipulation while matching the mechanical demands of the tissue. Finally, scaffold architecture is critical, an interconnected porous matrix with high porosity is essential to facilitate cell infiltration, tissue ingrowth, and the diffusion of nutrients and waste [9-15].

Typically, three groups of biomaterials have been used in the fabrication of scaffolds for TE: ceramics, synthetic polymers and natural polymers [9]. Each one of these has specific advantages and disadvantages, so the use of composite scaffolds comprised of different phases has been a common trend in TE [16]. Ceramic scaffolds such as hydroxyapatite and tri-calcium phosphate have been used for harder tissues, usually bone, since they are characterized for their high Young's Modulus and have low elasticity [14]. Synthetic polymers like polystyrene, poly-l-lactic acid and others, can be fabricated with a tailored architecture and their degradation characteristics controlled by varying the polymer itself, but they have a higher risk of rejection since their biocompatibility is lower [17]. There have also been some concerns about these types of scaffolds' degradation by-products as they degrade by hydrolysis, producing carbon dioxide, lowing the local pH which can lead to necrosis [17]. The last common approach is with biological materials such as collagen, alginate-based substrates and chitosan [13-19]. They are biologically active and typically promote excellent cell adhesion and growth, while also being biodegradable, but they usually have poor mechanical properties, facing challenges in harder tissues TE, and the architecture is very heterogeneous, making it harder to reproduce [4-15].

Even today, TE continues to face major obstacles, particularly the lack of biomaterials that can effectively support cell growth and function while closely replicating the native characteristics of the target tissue [13]. Achieving similarity in architecture and mechanical properties is critical for ensuring both biological functionality and overall substitute performance. Nanotechnology, especially using nanoparticles (NPs) such as silver NPs, gold NPs, titanium dioxide (TiO_2) NPs [20], or the use of electrospun nanofibers, nanostructured substrates and self-assembly nanomaterials [21], has gained attention as a promising strategy to address these limitations. Polymer-based nanocomposites offer distinct advantages, as the incorporation of NPs strengthens the material and provides essential biophysical cues. This enhancement improves both mechanical and biological performance, creating a more favourable environment for interactions between cells and the ECM, ultimately shaping cellular behaviour [4], [9], [15].

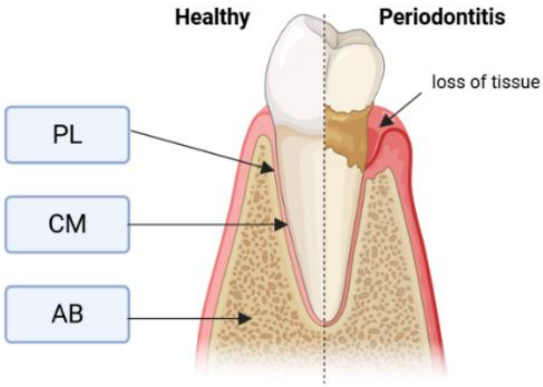

Figure 1: Healthy Vs Unhealthy periodontal tissues. Image created using BioRender (https://www.biorender.com/).

1.2 Alginate Scaffolds

Alginate is a naturally derived polysaccharide obtained from brown algae and can also be produced by bacteria such as *Pseudomonas* and *Azotobacter* [22]. It is widely studied in biomedical applications due to its biocompatibility, low toxicity, and ability to form hydrogels under mild conditions. These properties, combined with its abundance and relatively low cost, have led to its extensive use in scaffold fabrication and TE [23-25].

Alginate is a linear copolymer composed of 1,4-linked β-D-mannuronic acid (M) and 1,4-linked α-L-guluronic acid (G) [23-26]. Its structure includes regions of consecutive M residues (M blocks), consecutive G residues (G blocks), or alternating M and G residues (MG blocks). It is available in various forms differing in purity, molecular weight, and viscosity, ranging from non-biomedical to biomedical grade [23-26]. Alginate is hydrophilic, water-soluble, and increases viscosity under neutral aqueous conditions. It forms hydrogels in the presence of polyvalent cations and exhibits a pH-dependent anionic character, allowing interactions with cationic polyelectrolytes, making them a convenient material for cell encapsulation and drug delivery [23-26]. Although alginate may contain variable endotoxin levels depending on its purification, it is generally biocompatible and safe for medical use. Research has explored alginate-based hydrogels and scaffolds as platforms for dermal applications, controlled release of bioactive agents, cancer therapy, and antimicrobial treatments [23-28]. These advances have enabled the development of highly tailored and complex systems that support tissue repair and regeneration. Their properties can be further enhanced by external stimuli or chemical functionalization, improving mechanical performance [23-26].

Alginate hydrogels mimic the ECM of living tissues, making them highly versatile for medical applications. Specifically, they have shown promise in periodontal TE, due to their ability to support both soft and hard periodontal tissue regeneration [24]. Alginate has been employed in periodontal TE [29-31] through approaches like the use of bioactive-modified alginate with sequential growth factors like Insulin-like Growth Factor 1 (IGF-1) and Bone Morphogenic Protein 6 (BMP-6) that have strong regenerative and anabolic effects [29], emulsion electrospun polylactic acid/alginate nanofibers which are mechanically stable, and have the ability to deliver healing molecules [30], or composites of alginate-nano bioactive glass which can combine soft tissue support with bone-regenerative cues [31].

These highly porous scaffolds possess unique mechanical properties, including shape-memory, which makes them particularly attractive for implantation in load-bearing sites, as they can recover their original shape after deformation [24-32]. Such scaffolds can be created by covalently crosslinking alginate through carbodiimide chemistry and can be engineered to display anisotropic properties. These anisotropic scaffolds have been specifically developed for the periodontium to replicate the structural features of the tissues [24-32].

1.3 TiO_2 in Tissue Engineering

NPs possess unique physical and chemical characteristics that enhance their performance in diverse applications, particularly TE. Their small size confers a high surface-to-volume ratio, slow sedimentation rates, and colloidal stability, allowing them to remain suspended in solution for extended periods. In TE, these features contribute to improved mechanical and biological performance of

scaffolds and biomaterials [20]. Gold NPs are widely used in TE due to their surface conjugation abilities and electrical conductivity [33-34]. Silver NPs, along with other metallic NPs and metal oxides, are valued for their strong antimicrobial properties [35-36]. Quantum dots offer unique fluorescence characteristics, while carbon nanotubes are known for their electromechanical behaviour [37-38]. Together, these properties make these nanomaterials highly useful for a huge range of TE applications. Additionally, magnetic nanoparticles have been employed in studying cell mechanotransduction [39], enhancing gene delivery, directing cell patterning, and facilitating the construction of complex 3D tissue structures [20], [40-41].

TiO_2 is a well-established ceramic nanomaterial belonging to the class of metal oxide nanostructures. It naturally occurs in four polymorphic forms: anatase (tetragonal), brookite (orthorhombic), rutile (tetragonal), and TiO_2(B) (monoclinic) [42-43]. Anatase, brookite and rutile are the most common forms. Structurally, these phases can be described in terms of chains of TiO_6 octahedra, where a central Ti^{4+} ion is coordinated by six O^{2-} ions [43]. In anatase, the Ti-Ti atomic distance is greater, while the Ti-O bond length is shorter compared to rutile. Additionally, the anatase lattice is more elongated along its crystallographic axis [43]. These structural distinctions lead to variations in density and electronic band structure [43]. The anatase phase exhibits an optical bandgap (Eg) of approximately 3.2 eV with an absorption edge at 388 nm, within the ultraviolet (UV) range (100-400 nm). Rutile, by contrast, has a slightly narrower bandgap of 3.02 eV, corresponding to an absorption edge at 410 nm that extends into the visible spectrum (400-700 nm) [43]. The differences in bandgap between anatase and rutile are crucial, as they determine photocatalytic efficiency, antibacterial activity, and stability, directly impacting their suitability for different applications [43-45].

Within the context of TE, TiO_2 NPs offer several advantageous properties, including biocompatibility, chemical stability, and inertness. The anatase phase is generally favoured in TE [46-47]. Their photocatalytic activity, highly influenced by the wider bandgap, has also been linked to antibacterial and antiseptic effects, as the generation of oxygen free radicals induces oxidative stress in microbial cells [42-43]. Coating, incorporation or surface functionalization are processes that can be applied to TiO_2 NPs to improve their biological properties [48-49]. Furthermore, the high surface area of TiO_2 NPs enhances cell adhesion and proliferation, making them suitable for incorporation into biodegradable polymer matrices [50].

Several metallic elements can be used in TE, like magnesium (Mg), calcium, iron, nickel, and others [51]. Mg has a close Young's Modulus to natural bone (at 41-45 GPa) and density, which avoids the phenomenon of stress shielding in the surrounding tissues [52]. Mg is the second most abundant intracellular cation, scientific evidence indicates that Mg in the body is distributed in a way that half is found in soft tissues and half in the bones [52], meaning it is biocompatible. Beyond that, Mg plays an essential role in bone metabolism, stimulating osteoblast activity, ECM synthesis, and mineralization, thus supporting periodontal regeneration [53-54]. When incorporated into TiO_2, Mg can alter the surface properties and biological response of the material which may be crucial for cell adhesion and proliferation [55].

In addition to improving biological performance, TiO_2 NPs can reinforce the mechanical properties of composites. They contribute to enhanced bending strength and Young's modulus, reaching values comparable to those of natural bone, while also providing bioactivity, as displayed in **Figure 2**.

Consequently, TiO_2 is widely investigated as a functional nanomaterial in bone TE, with potential for scaffold design in periodontal TE [56-57].

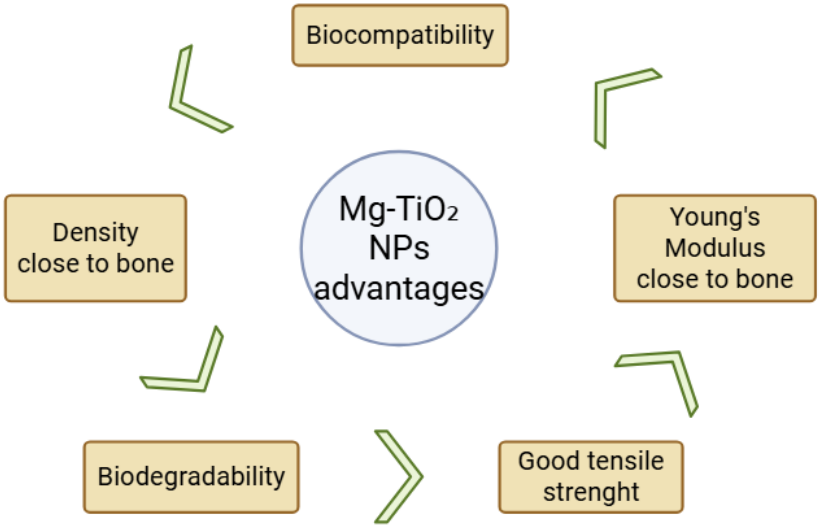

Figure 2: Mg-TiO_2 NPs advantages for TE. Image created using BioRender (https://www.biorender.com/).

1.4 Hypothesis and Aim

The limited regenerative capacity of periodontal tissues, particularly AB and PL, has led to increasing need for advanced biomaterials capable of supporting predictable regeneration, especially in coordinating the regeneration between all the different types of tissues in the periodontium [58]. Current scaffold-based and pharmacological strategies, although somewhat effective, often lack sufficient osteoinductive properties and fail to restore the structural and functional complexity of the periodontal tissues [58]. TiO_2 NPs have been extensively explored in biomedical research due to their biocompatibility, antimicrobial properties, and ability to support cell adhesion and proliferation [59]. However, their osteoinductive potential remains limited, and further functionalization is required to enhance their suitability for regenerative applications. Mg represents an attractive element for incorporation due to its abundance in the human body (approximately 60 to 65% [60]), established role in bone metabolism, and ability to promote osteogenesis [61]. Integrating TiO_2 NPs with Mg is expected to improve their bioactivity, enhance surface properties, and stimulate cellular responses. Despite these promising attributes, investigations into Mg-TiO_2 NPs for TE and particularly in periodontal regeneration remain significantly scarce, emphasizing the innovative aspect of the present work.

Moreover, conventional chemical synthesis of NPs often requires toxic reagents and high energy inputs, raising concerns over environmental impact and clinical translation, meaning the unsafety of moving it towards practical use in patients [62-63]. To address this, we propose the use of microwave-assisted irradiation as a sustainable and safer synthesis strategy. This approach allows for rapid, energy efficient, and solvent minimized production of NPs with controlled crystallinity and morphology, aligning with sustainable principles while ensuring biomedical applicability [62-64].

The objective of this work is to develop Mg-TiO_2 NPs via a green microwave-assisted synthesis route and evaluate their potential as functional nanofillers for periodontal TE alginate scaffolds. We hypothesized that firstly, Mg incorporation will improve the biological activity of TiO_2 NPs, secondly, microwave-assisted synthesis will provide a sustainable and reproducible route to produce NPs with desirable physicochemical properties, and thirdly the resulting Mg-TiO_2 NPs will enhance scaffold performance by improving mechanical stiffness and promoting osteogenic differentiation, ultimately contributing to predictable regeneration of periodontal tissues.

2

MATERIALS AND METHODS

This chapter is organized in two main sections. The first section focuses on the production, optimization, and characterization of the NPs. The second section describes the synthesis and comprehensive characterization of the various scaffold types.

2.1 TiO_2 Nanomaterials synthesis

TiO_2 NPs were synthesized with a microwaved-assisted hydrothermal method, adapting a process described in *Matias et al* [65]. To obtain the solution, 1.6 mL of titanium (IV) isopropoxide ($C_{12}H_{28}O_4Ti$; 97%; CAS: 546-68-9; Sigma-Aldrich) was added drop by drop to 48.4 mL of ethanol, the solution was then stirred until it was homogeneous. To prepare the TiO_2 NPs with Mg incorporated, 5 mol. %, 7 mol. % and 10 mol. % of magnesium nitrate-6-hydrate ($Mg(NO_3)_2(H_2O)_6$; ≥ 98%; CAS: 13446-18-9; Panreac) was added to the previous solution and stirred again. The mixed solution was then put in two Teflon vessels, each one with 25 mL of solution and then carried to the CEM MARS one microwave digestion system (CEM, Matthews, USA) to synthesize the NPs. The parameters of the microwave were divided in two stages, using 900 W. The first one started with a ramp of 5 minutes, to reach 150 ºC, with a hold time of 15 minutes. The second one had a ramp of 15 minutes to reach 210 ºC, and then the process took place for 1 hour. The resulting NPs were centrifugated and washed for 5 minutes each time, at 5000 rpm, two times using water and two times using isopropyl alcohol (IPA). For an eco-friendly drying process, the NPs were air-dried for a few days at room temperature (RT).

Hereafter, the nanomaterials are named as intrinsic TiO_2, 5, 7 and 10 mol. % Mg-TiO_2.

2.1.1 Characterization Techniques

2.1.1.1 X-Ray Diffraction (XRD)

To identify the crystalline structure of the NPs, XRD experiments were carried in Bench XRD AERIS Malvern PANalytical B.V.. The obtained crystalline phases were compared to datasheets from the International Centre for Diffraction Data (ICDD). The reference code for the anatase structure is 00-021-1272, for the rutile structure is 04-008-7850, and for the brookite structure is 04-008-7851. CuKα radiation source (λ=1.54060 Å). The data was collected in a range of 10º to 90º (2Θ) with a scanning step of 0.02º, rotation of 0.25º, and a time per step of 45 s.

Average crystalline size (τ) of the samples was calculated using the Debye-Scherrer equation (**Equation 1**) [66].

$$\tau\,(\mathrm{nm}) = \frac{K\lambda}{\beta\cos(\theta)} \quad (1)$$

Where K corresponds to the shape factor, with a value close to unity (usually 0.9), λ is the X-Ray wavelength, β is the line broadening at half the maximum intensity (FWHM) after subtracting the instrumental line broadening, in radians, and θ is the Bragg angle, also in radians.

The lattice parameters were determined using X'Pert HighScore Plus software, following calibration with standard silicon (Si) reflections (reference code 00-027-1402).

2.1.1.2 Raman Spectroscopy

To have detailed insights of the vibrational and structural properties and therefore identify the crystal phase of the NPs, Raman spectroscopy was conducted in a backscattering configuration using the 532 nm laser of the Raman Microscope Reninshaw Qontor, utilizing a grating density of 1200 grooves/nm and equipped with objective lens of 50x.

2.1.1.3 Optical Characterization

The absorbance measurements were obtained by using a double-beam Ultraviolet-Visible-Near Infrared (UV-Vis-NIR) Shimazu spectrophotometer with an integrated sphere with a range of 280 to 800 nm. The data were recorded at RT and $BaSO_4$ powder was used as a reference.

The optical bandgap energy (Eg) was determined from the UV-VIS data using the Tauc relation, expressed in **Equation 2** [67]**.**

$$(\alpha h\nu)^m = A(h\nu - Eg) \quad (2)$$

Where α represents the absorption coefficient hν is the photon energy, A is a proportionality constant, and m is an exponent that defines the nature of the electronic transition: m= 2 for direct allowed transitions and $m = \frac{1}{2}$ for indirect allowed transitions. The Eg was obtained by extrapolating the linear portion of the $(\alpha h\nu)^m$ versus hν plot to the intercept at $(\alpha h\nu)^m = 0$. Since anatase TiO_2 exhibits an indirect bandgap, $m = \frac{1}{2}$ was applied [67], [68].

2.1.1.4 Electron Microscopy

Scanning electron microscopy (SEM) was carried out using a Hitachi Regulus 8220 microscope equipped with an Oxford Instruments energy-dispersive X-ray spectrometer (EDS). Scanning Transmission Electron Microscopy (STEM) analyses, including high-angle annular dark-field (HAADF) imaging, were performed on a Hitachi HF5000 field-emission transmission electron microscope operated at 200 kV. This probe-corrected instrument, equipped with a cold field-emission gun (FEG), featured a 100 mm^2 Oxford Instruments EDS detector. For specimen preparation, a drop of the sonicated dispersion was deposited onto a lacey-carbon copper grid and dried in air. The mean TiO_2 particle size was estimated from SEM and STEM images by measuring the dimensions of 30 individual NPs.

2.1.1.5 Brunauer-Emmett-Teller (BET) analysis

The specific surface area was estimated through nitrogen (N_2) adsorption-desorption, according to the BET method at 77 K and applied within the p/p0 range as specified in ISO-9277 [69]. An Autosorb IQ ad sorption apparatus from Quantachrome (Florida, USA) was employed. Before the experiments, ≈ 0.2 g of TiO_2 and 10 mol.% Mg-TiO_2 NPs were outgassed for 6 h at 120 °C (5°C min^{-1}).

2.2 Alginate Scaffolds synthesis

The alginate scaffolds were made by adapting a process detailed in *Almeida et al* [32]. 0.1 M of 2-(N-Morpholino) ethanesulfonic acid buffer (MES; ≥ 99%; CAS: 4432-31-9; Sigma Aldrich) and 0.2 M of sodium chloride (NaCl; ≥ 99.5%; CAS: 7647-14-5; Panreac AppliChem) were added in 20 mL of distilled water and stirred. Then, sodium alginate (COO^-; CAS: 9005-38-3; Sigma-Aldrich) was dissolved for 3 hours with a concentration of 4.5% (w/v). 1-ethyl-3-dimethraminopropyl carbodiime (EDAC; CAS: 25952-53-8; Sigma-Aldrich) and N-Hydroxy-succinimide (NHS; ≥ 97.5%; CAS: 6066-82-6; Sigma-Aldrich) were added and stirred for 20 minutes to a final molar ratio of 2:1:2 EDAC: NHS: COO^-. After, adipic acid dihydrazide (AAD; ≥ 98%; CAS: 1071-93-8; Sigma-Aldrich) was added in an aqueous solution to a ratio of 45%, compared to the alginate (nNH_2/nCOOH= 45%), and was quickly stirred until homogenised. The resultant solution was then placed into a petri dish, for the crosslinking reaction to occur during the night at RT. To wash the obtained hydrogels, 0.1 M calcium chloride aqueous solution ($CaCl_2$; CAS; ≥ 97%; 10043-52; Fluka) was added to get an extra ionic crosslinking, an orbital shaker was used to stir the petri dish for 2 hours. The last washing step was to add the distilled water in the petri dish for 24 hours. The hydrogel was sectioned into small pieces using a biopsy punch (6 mm of diameter). The resulting structures were rapidly frozen by immersion in liquid nitrogen and subsequently stored at -80 °C. Following storage, the scaffolds were subjected to freeze-drying for 24 hours using a Benchtop Freeze Dryer (Labconco), operating at -45 °C under vacuum conditions.

2.2.1 Nanoparticles incorporation

To incorporate the NPs in the scaffolds, two different approaches were performed, blending and coating. The NPs chosen were the 10 mol. % Mg-TiO_2 NPs. The specific NPs condition was selected to maximize the adhesion and proliferation of cells.

To do the blending, an aqueous solution of 3 mL was prepared. 0.25% ($w/v_{Scaffold}$) of NPs were added to distilled water and then the solution was stirred for 15 minutes. The resulting solution was added to the precursor solution between the step of adding EDAC and NHS, allowing the NPs to be directly incorporated in the scaffold's matrix. The rest of the synthesis was identical.

For the coating, a suspension of the NPs was prepared. An aqueous solution of Polyethylenglycol 3400 (PEG 3400; $H(OCH_2CH_2)_nOH$; CAS: 25322-68-3; Sigma-Aldrich), with a concentration of 0.2 mg/mL, was dissolved for 24 hours. Another solution was prepared, by mixing the NPs in 3 mL of IPA, with a NPs concentration of 0.25% ($w/v_{Scaffold}$), which was left in an ultrasonic bath for 30 minutes. Finally, 1.8 mL of the first solution was mixed with the second, and this final mix was left stirring for 6 hours, at 50 ºC. A drop of this final solution (≈ 20 µL) was applied to the scaffolds with a micropipette.

The resulting scaffolds were left to dry, while the drop of solution was absorbed. The rest of the synthesis was identical. In **Appendix A.4** is a picture of the scaffolds.

In **Figure 3**, a schematic of the scaffold's fabrication process is represented

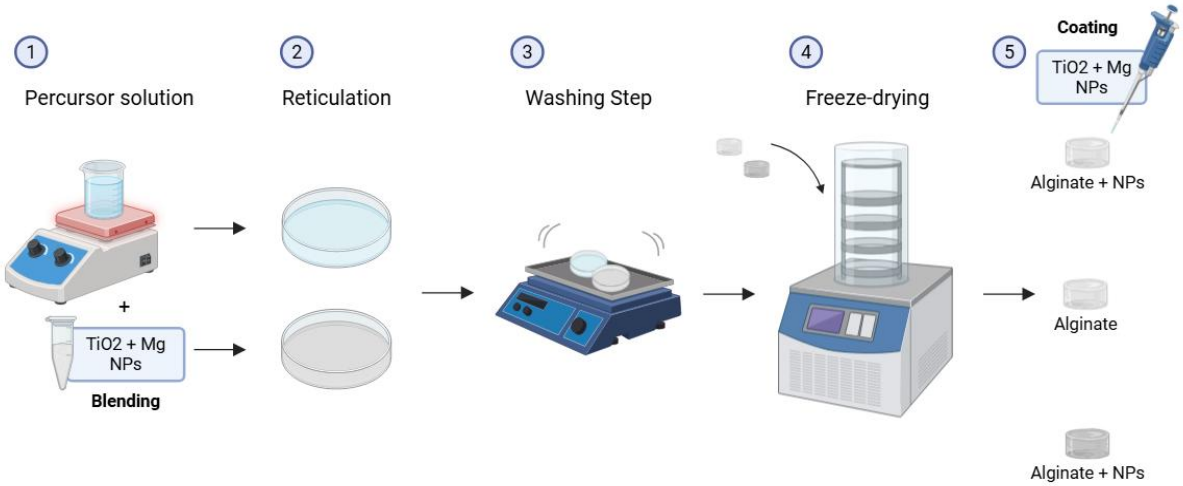

Figure 3: Preparation of the different types (pristine, coating and blending of NPs) of scaffolds. Image created using BioRender (https://www.biorender.com/).

2.2.2 Characterization Techniques

2.2.2.1 Morphological Characterization

SEM was performed to examine the scaffolds' fine structure and surface details (pore architecture and surface texture). Additionally, EDS was used to analyse the elemental composition and verify NPs incorporation in both the scaffolds with coating and scaffolds with blending.

To obtain the scaffold's porosity (P), **Equation 3** was used [70].

$$P\ (\%) = \left(1 - \frac{\rho_{scaffold}}{\rho_{material}}\right) \times 100 \qquad (3)$$

Where $\rho_{scaffold}$ is the density of the produced scaffolds, calculated from the values of mass and volume of the dry hydrogels, and $\rho_{material}$ is the theoretical density (the value for the utilized sodium alginate is 1 g/cm^3). The calculations were made with 3 samples (3 replicates, n=3).

2.2.2.2 Swelling Behaviour

To evaluate the swelling behaviour, the dry scaffolds were first weighed to obtain their initial mass (W_0). They were then immersed in a phosphate-buffered saline (PBS) solution (pH ≈ 7) and kept submerged for a total of 7 days. At specific time intervals of 1 hour, 2 hours, 3 hours, 1 day, 2 days, 3

days, 6 days and 7 days, the scaffolds were removed, gently blotted to eliminate excess PBS, and re-weighed to determine their swollen mass (W_t) [71].

The recorded mass values were then used in **Equation 4** to generate swelling kinetic curves for the three scaffold types under investigation [71]. Each experiment was performed in triplicate (n=3).

$$\text{Water Uptake (\%)} = \frac{W_t - W_0}{W_0} \times 100 \quad (4)$$

2.2.2.3 Mechanical Essay

Compression tests were performed at RT using the Electromechanical and Ambiental Test Machine (AUTOGRAPH AGX-V Series, SHIMADZU) instrument equipped with a 1000 N load cell. All scaffold types produced were evaluated under compression at a displacement rate of 1 mm/min. None of the samples collapsed during testing. The Young's modulus was determined from the initial linear region of the stress(σ)-strain(ε) curves, following **Equation 5**. Each test was carried out in triplicate (n=3), using wet scaffolds that had been pre-soaked in PBS for 24 hours.

$$\text{E (kPa)} = \frac{\sigma}{\varepsilon} \quad (5)$$

2.2.2.4 Cell Viability (Live/dead Essay)

Cell viability was assessed in all types of scaffolds, the experiment was done in triplicate (n=3). Prior to cell seeding and viability test, all scaffolds were immersed in ethanol for 15 minutes to verify their structural stability and ensure they did not disintegrate upon contact with the solvent.

Saos-2 cells (ATCC HTB-85), a human osteosarcoma cell line capable of differentiating into osteoblast cells, expanded in a growth medium (High-Glucose DMEM, 10% Fetal Bovine Serum, 1% Pen/Strep), under standard conditions (37 °C, 5% CO_2, humidified atmosphere) until reaching the desired confluence. The working solution was prepared, consisting of 2 µM Calcein-AM and 4 µM Propidium Iodide (PI) in PBS. The culture medium was removed, and the cells were washed with PBS. Then, the staining solution was added to completely cover the samples. Cells were incubated for 15-30 minutes at 37 °C, protected from light. After incubation, samples were rinsed with PBS and immediately examined under a fluorescence microscope. Viable cells were marked by Calcein-AM (cyan fluorescence) and non-viable cells by PI (magenta fluorescence). Images were acquired using a confocal microscope and processed with ImageJ to quantify live/dead ratios as well as cell count to estimate the viability using **Equation 6** [72].

$$\text{Cell Viability (\%)} = \frac{N_{viable}}{N_{viable} + N_{non-viable}} \times 100 \quad (6)$$

2.2.2.5 Statistics

Statistical analyses were performed using GraphPad Prism 10 software. Data are presented as mean ± standard deviation (SD). The number of replicates (n) were always 3. Normality of the data was assessed using the Shapiro-Wilk test, while homogeneity of variance was verified with Levene's test. One-way ANOVA and Two-way ANOVA were applied to evaluate statistical significance within datasets, followed by Tukey's HSD post-hoc test to identify differences between groups. Statistical significance was defined as *$p < 0.05$, with increasing levels of significance denoted as **$p < 0.01$ (very significant), ***$p < 0.001$ (highly significant), and ****$p < 0.0001$ (extremely significant).

3

RESULTS AND DISCUSSION

3.1 TiO_2 Nanomaterials

3.1.1 XRD

The synthesized NPs were investigated using XRD and the results are shown in **Figure 4**. All peaks in the experimental diffractograms indicate the presence of TiO_2 anatase phase. The peaks detected correspond to the reflections (101), (004), (200), (105), (211), (204), (116), (220) and (215) at 2θ = 25.3, 37.8, 48.0, 53.8, 54.9, 62.8, 68.9, and 75.0º, respectively [73]. No reflections associated with rutile or brookite were detected in any of the samples. For the Mg-rich nanostructures, no peaks assignable to a metal oxide phase were detected, but there is a slight shift of the peaks. Nevertheless, except for the (004) reflection, which showed a shift toward higher 2θ values in all Mg-containing samples compared to the intrinsic material, all other reflections exhibited a shift towards lower 2θ values, except the (105), (116), and (215) reflections, which remained unchanged upon Mg addition. This behaviour can be explained by the substitution of Ti^{4+} by Mg^{2+} in the anatase lattice [74]. Although Mg^{2+} has a larger ionic radius (≈ 0.720 Å) compared to Ti^{4+} (≈ 0.605 Å), its substitution into the TiO_2 lattice introduces lattice strain due to the size mismatch, which tends to expand the lattice in the basal plane (a) [74]. Additionally, because Mg^{2+} has a lower valence than Ti^{4+}, the crystal compensates for the charge imbalance by forming oxygen vacancies or reducing Ti^{4+} to Ti^{3+} [74]. These point defects induce further lattice distortion that can counteract the expansion and cause some contraction in the plane c-axis [74]. The combination of these effects results in anisotropic lattice distortions, consistent with the observed peak shifts [74-78]. To confirm this, the lattice parameters were calculated using X'Pert Highscore Plus software, which is summarized in **Table 1**, Si was used as an internal standard to accurately calibrate the diffraction data and to confirm that the observed peak shifts in the NPs are effectively associated with Mg incorporation.

As shown in **Table 1**, the lattice parameter a (= b) increased slightly overall with the increase of Mg incorporation, while the lattice parameter c had an inverse tendency, it decreased. This behaviour is typical of substitutional incorporation, where Mg^{2+} replaces Ti^{4+} [77]. The increase in the average ionic radius led to an expansion in the basal plane (a), while the cell compensated with a slight contraction along c, keeping the overall volume stable, as we can confirm by the a/c ratio relatively constant.

This suggests that Mg was incorporated into the anatase crystal lattice, slightly modifying the anisotropy of the unit cell, causing the shifts in the XRD peaks.

The estimated crystalline sizes (τ) are summarized in **Table 2**, calculated using **Equation 1**. The reduction in τ with the increased Mg content suggests that Mg acts as a growth inhibitor, likely by substituting Ti^{4+} ions in TiO_2 lattice and introducing lattice distortion. This decrease may enhance properties such as surface area and adsorption capacity, which is consistent with reports in literature, where Mg incorporation into the lattice has been shown to effectively limit crystal growth and modify the microstructure of TiO_2 NPs [79-80].

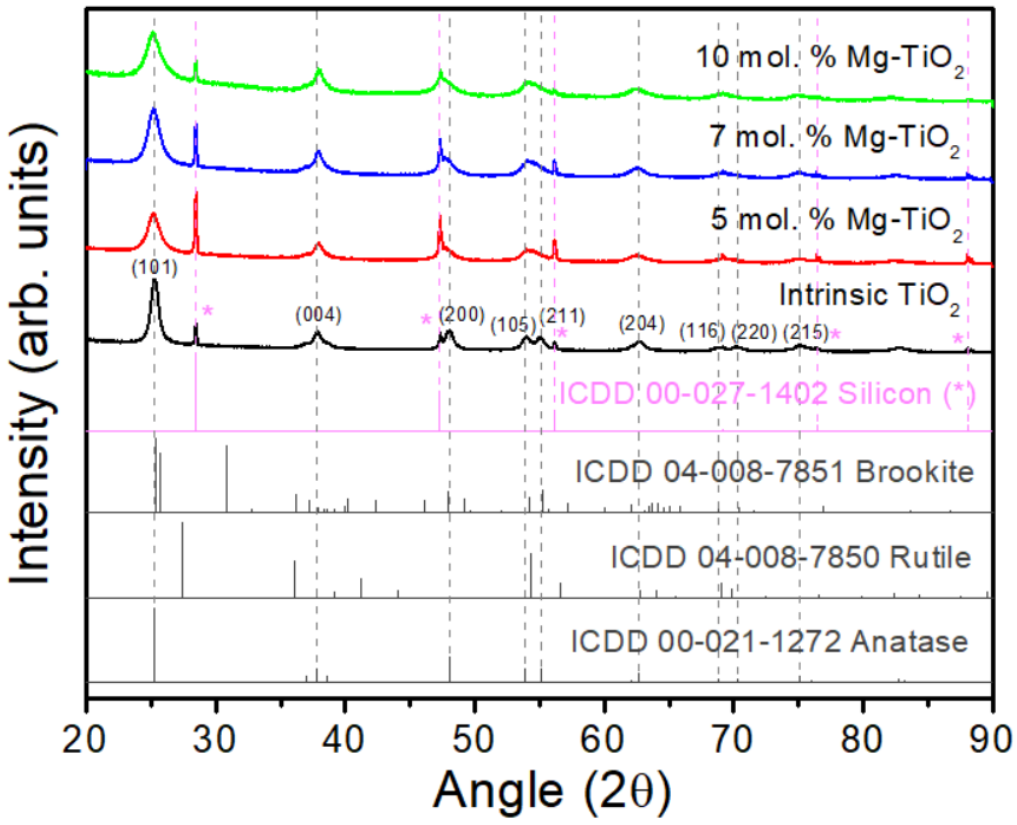

Figure 4: XRD diffractograms of the synthesized TiO_2 nanomaterials. Intrinsic TiO_2 NPs, 5, 7 and 10 mol. % Mg-TiO_2. ICDD reference patterns for the anatase, rutile and brookite phases and standard Si (marked as *).

Table 1: Lattice parameters of intrinsic TiO_2 and 5, 7 and 10 mol. % Mg-TiO_2 NPs.

	a = b (Å)	**c (Å)**	**a/c (ratio)**
Intrinsic TiO_2	3.782	9.510	0.397
5 mol. % Mg-TiO_2	3.790	9.460	0.401
7 mol. % Mg-TiO_2	3.790	9.490	0.399
10 mol. % Mg-TiO_2	3.792	9.460	0.401

Table 2: Estimated crystalline sizes (nm) for intrinsic TiO_2 and 5, 7 and 10 mol. % Mg-TiO_2 NPs.

	TiO_2	**5 mol. % Mg-TiO_2**	**7 mol. % Mg-TiO_2**	**10 mol. % Mg-TiO_2**
τ (nm)	10.03 ±0.02	7.37 ±0.11	7.33 ± 0.11	6.78 ± 0.09

3.1.2 Raman Spectroscopy

The Raman spectra of the different phases of TiO_2 are considerably different, so this is a powerful technique to distinguish them [81-82]. TiO_2 Raman bands appear in between the 100-700 cm^{-1} range. Five bands corresponding to four characteristic active modes of the tetragonal anatase phase can be observed in **Figure 5**, with symmetries Eg, B_{1g}, A_{1g}, and Eg, at 145, 395, 515 and 640 cm^{-1}, respectively [73]. These vibrational frequencies and their intensity ratios confirm the phase anatase of TiO_2.

No additional peaks related to Mg or Mg oxides were detected in the Mg-TiO_2 samples, which corroborates the results of XRD.

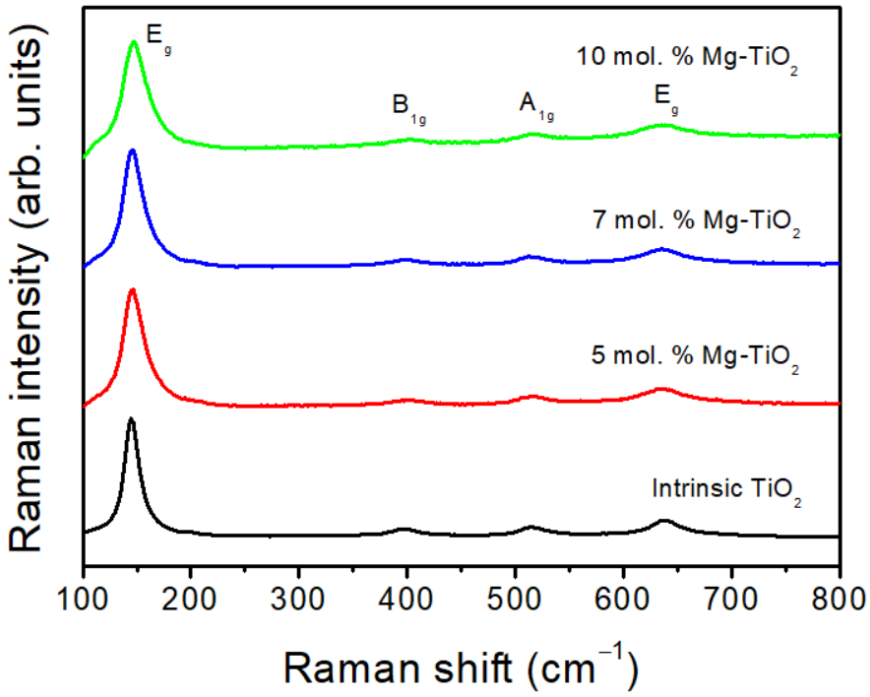

Figure 5: Raman spectra of the synthesised TiO_2 nanomaterials. Intrinsic TiO_2 NPs, 5, 7 and 10 mol. % Mg- TiO_2.

3.1.3 Optical Characterization

To investigate the optical absorption characteristics of intrinsic TiO_2 and Mg-TiO_2 nanostructures, UV-VIS absorption spectra were recorded. **Figure 6** reveal a pronounced absorption edge in the UV region in all samples which is characteristic of TiO_2 [83]. The absorption maximum for the intrinsic TiO_2 was ≈ 336 nm (around 3.69 eV) and for 5, 7 and 10 mol. % Mg-TiO_2 were ≈ 318 nm (around 3.90 eV). The addition of the Mg content resulted in a slight blue shift of the absorption edge.

The corresponding Tauc plots (**Figure 7**) were used to estimate the Eg energies using **Equation 2**. The TiO_2 nanopowders exhibited significant sub-bandgap absorption, which prevented the determination of Eg from the x-intercept of a single linear fit [84]. Therefore, an additional linear fitting to the broader bandgap region was performed, and Eg was obtained from the intersection of the two linear fits, resulting in values of approximately 3.05 eV for intrinsic TiO_2, 3.10 eV for 5 mol. % Mg-TiO_2, 3.13 eV for 7 mol. % Mg-TiO_2 and 3.10 eV for 10 mol. % Mg-TiO_2 [84]. Although anatase TiO_2 typically exhibits an Eg of 3.2 eV, the TiO_2 nanopowders showed a slightly lower value. Previous studies conducted by *Guan et al* [85] and *Choudhury et al* [86] observed that the formation of oxygen vacancies introduced

localized electronic states within the bandgap, enabling optical transitions at lower photon energies and consequently reducing the apparent Eg [83]. The incorporation of Mg^{2+} ions likely substituted Ti^{2+} sites in the TiO_2 lattice, leading to a reduction in defect-related states, which may explain the observed variation in Eg with Mg concentration [87]. However, it is relevant to note that the true Eg values remain uncertain due to estimation errors using the Tauc method [67], [88].

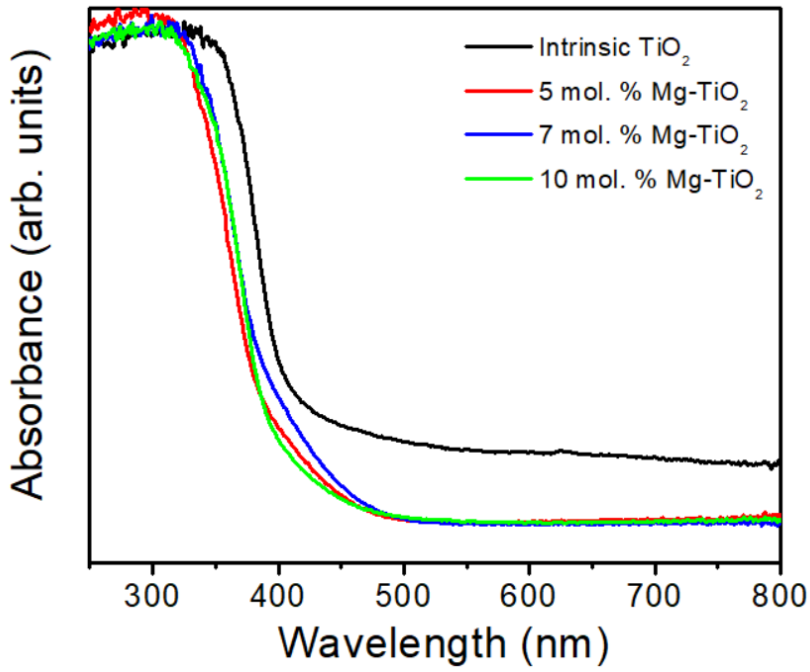

Figure 6: Optical characterization of the TiO_2 nanomaterials. UV-VIS spectra of the intrinsic TiO_2, 5, 7 and 10 mol. % Mg-TiO_2.

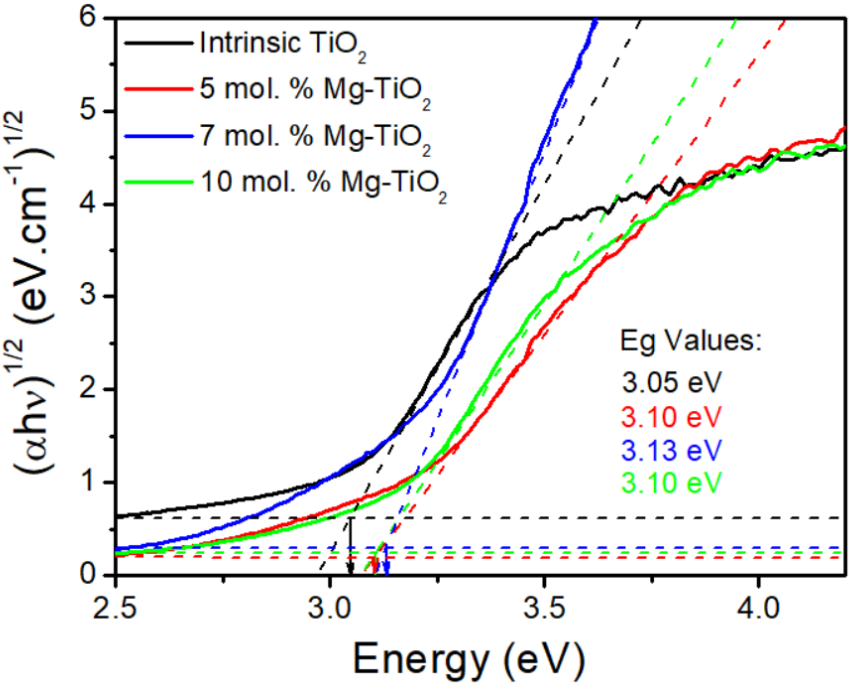

Figure 7: Optical characterization of the TiO_2 nanomaterials. Bandgap calculation via Tauc equation for intrinsic TiO_2, 5,7 and 10 mol. % Mg-TiO_2.

3.1.4 Electron Microscopy

Figure 8 presents SEM images of TiO_2 nanopowders, with and without Mg incorporation, synthesized by microwave irradiation. In both cases, the powders consist of spherical aggregates, with average aggregate sizes of 87.21 ± 19.75 nm for TiO_2 and 193.66 ± 18.15 nm, 203.52 ± 32.68 nm and 311.20 ± 15.34 nm for the 5, 7 and 10 mol. % Mg-TiO_2 nanopowders, respectively. These values align with what has been reported in literature [89-90]. Minimum, maximum and average size of the NPs as well as the size variation (Δ) is summarized in **Table 3**. The Δ of the NPs indicates their heterogeneity, as they exhibit different sizes. This heterogeneity increased with the incorporation of Mg, which agrees with what has already been reported in literature [91]. This suggests that higher Mg concentrations may induce more heterogeneous nucleation and growth conditions.

For the pure TiO_2 and both 5 and 7 mol. % Mg-TiO_2 (**Figure 8, (a), (b) and (c)**) it can be observed square-shaped nanocrystals. The average nanocrystal sizes were 14.54 ± 2.06 nm for TiO_2, and 12.09 ± 1.38 nm and 11.36 ± 2.10 nm for 5 and 7 mol. % Mg-TiO_2, respectively. In the case of 10 mol. %, it is evident that as Mg amount has increased, it changed the shape of the nanocrystals, originating nanorods. The nanorod aspect ratio was 2.85, with an average length of 20.67 ± 4.42 nm, and diameter of 7.24 ± 0.76 nm. This demonstrates that Mg addition leads to a significant impact on TiO_2 nanostructure. This change in the TiO_2 NPs morphology with increasing Mg content is consistent with previously reported findings in literature, when an element with a larger ionic radius substitute into the lattice modifies the relative stability of the crystallographic planes [92-93]. When Mg^{2+} ions attach preferentially to a certain crystal plane of TiO_2, they make that surface more stable and less likely to keep growing. As a result, the crystal does not expand evenly in all directions, favouring one-dimensional crystal growth, leading to an elongated shape such as nanorods [84-86]. In addition, substitution of Ti^{4+} by Mg^{2+} introduces lattice strain and charge imbalance, which inhibit crystal growth and lead to a reduction in crystallite size. The concentration-dependent reduction in crystallite size originates directly from the combined effects of lattice strain, defect formation, and modified surface energetics induced by Mg incorporation [94-97].

The 10 mol. % Mg-TiO_2 nanomaterial was further investigated using the STEM microscopy and the results are presented in **Figure 9**. The aggregates and rod-like nanocrystals are clearly observed in **Figures 9 (a) and (b)**. An individual nanocrystal is shown in **Figures 9 (c) and (d)**, where structural surface defects and large voids are clearly visible. In **Figure 9 (d)**, the atomic columns can be observed; however, In the HAADF-STEM images (**Figure 9 (e)**), the presence of Mg atoms could not be distinguished. Observed along the [001] zone axis (inset in **Figure 9 (e)**), the FFT pattern displayed the characteristic 90° angle between the (200) and (020) planes of anatase (ICDD 00-021-1272). The presence of defects in TiO_2 nanocrystals synthesized under microwave irradiation have been reported previously [65], [98-99]. Microwave irradiation interacts with NPs, inducing surface defects and influencing their crystallography and morphology through several interrelated mechanisms. First, rapid volumetric heating allows microwaves to heat the NPs and precursors directly and extremely quickly [100-101]. This generates thermal gradients and localized lattice stresses, promoting the formation of oxygen vacancies and other structural defects [102-103]. Additionally, the fast, non-equilibrium crystal growth characteristic of microwave-assisted synthesis accelerates crystallization compared to conventional thermal methods [100-101]. The rapid growth limits full lattice relaxation, causing atoms to occupy non-ideal positions and generating both bulk and surface defects [100-103]. These structural modifications can

enhance surface bioactivity, protein adsorption, and cell-material interactions, which are particularly advantageous for TE applications [104].

Figure 10 shows the EDS maps of the 10 mol. % Mg-TiO_2 nanomaterial, and it is clear the homogeneous distribution of Ti, O and Mg, without any impurity detected. Surface defects were also observed in the nanocrystal investigated (**Figure 10 (a)**).

Table 3: Intrinsic TiO_2 and 5, 7 and 10 mol. % Mg-TiO_2 average dimensions. Obtained with ImageJ (n=30).

	Minimum Size (nm)	**Maximum Size (nm)**	**Average Size (nm)**	**Size Variation: Δ (nm)**
Intrinsic TiO_2	11.38	17.50	14.54±2.06	6.12
5 mol. % Mg-TiO_2	9.52	15.85	12.09±1.38	6.33
7 mol. % Mg-TiO_2	8.15	15.58	11.36±2.10	7.42
10 mol. % Mg-TiO_2	8.06	14.55	10.60±1.93	6.49

As expected, the obtained values for the average particle size (**Table 3**) are superior to the crystalline sizes (**Table 2**), since particles are agglomerates of grains, and the grains are composed of several crystallites [73]. This behaviour is commonly reported in literature, where the crystalline size of TiO_2 nanomaterials determined by XRD is smaller than the particle size measured by microscopic techniques [73], [105]. Such differences come from the fact that TiO_2 tends to agglomerate a lot during its synthesis due to their high surface energy, leading to a larger observed particle dimensions compared to the size of individual crystallites [105-106].

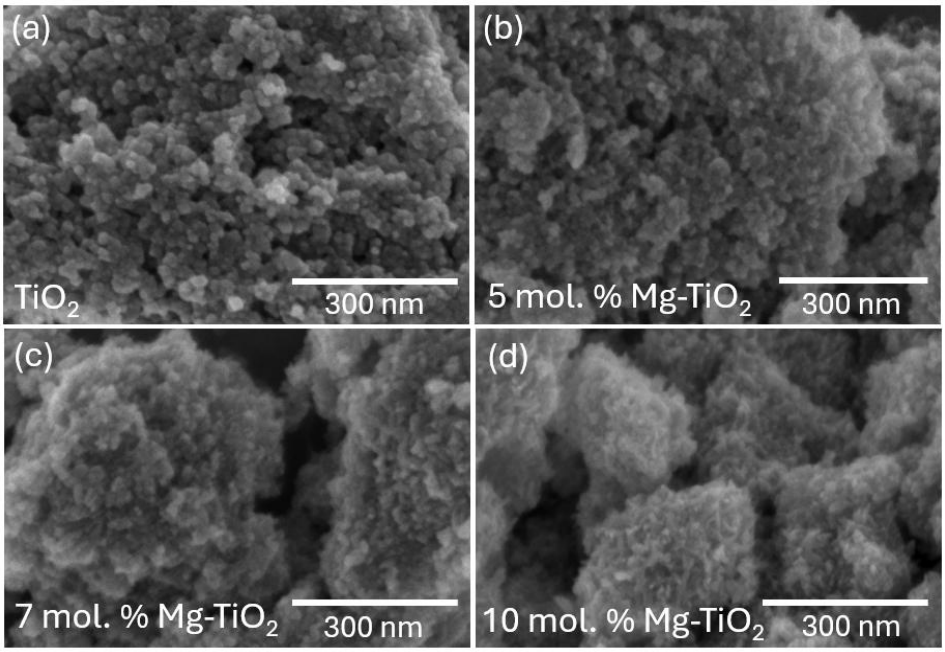

Figure 8: SEM morphological analysis of the TiO_2 NPs. (a) the TiO_2 NPs, **(b)** the 5 mol. % Mg-TiO_2 NPs, **(c)** the 7 mol. % Mg-TiO_2 NPs and **(d)** the 10 mol. % Mg-TiO_2 NPs. Scale bars represent 300 nm.

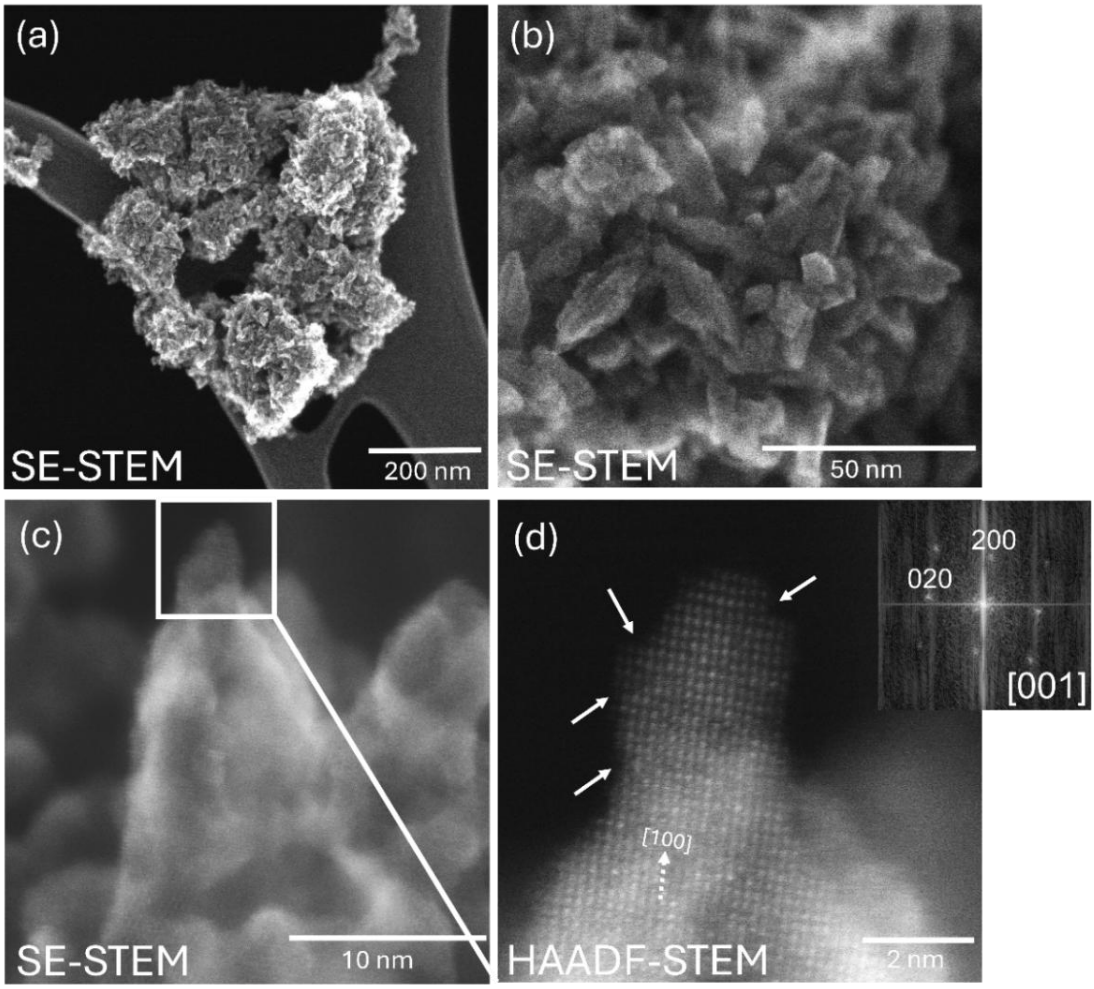

Figure 9: STEM analysis of the 10 mol. % Mg-TiO_2 nanopowder. (a) and **(b)** SE-STEM images of the Mg-TiO_2 aggregates and their rod-like structured nanocrystals, **(c)** SE-STEM and **(d)** HAADF-STEM images of an individual TiO_2 nanocrystal with the corresponding FFT image.

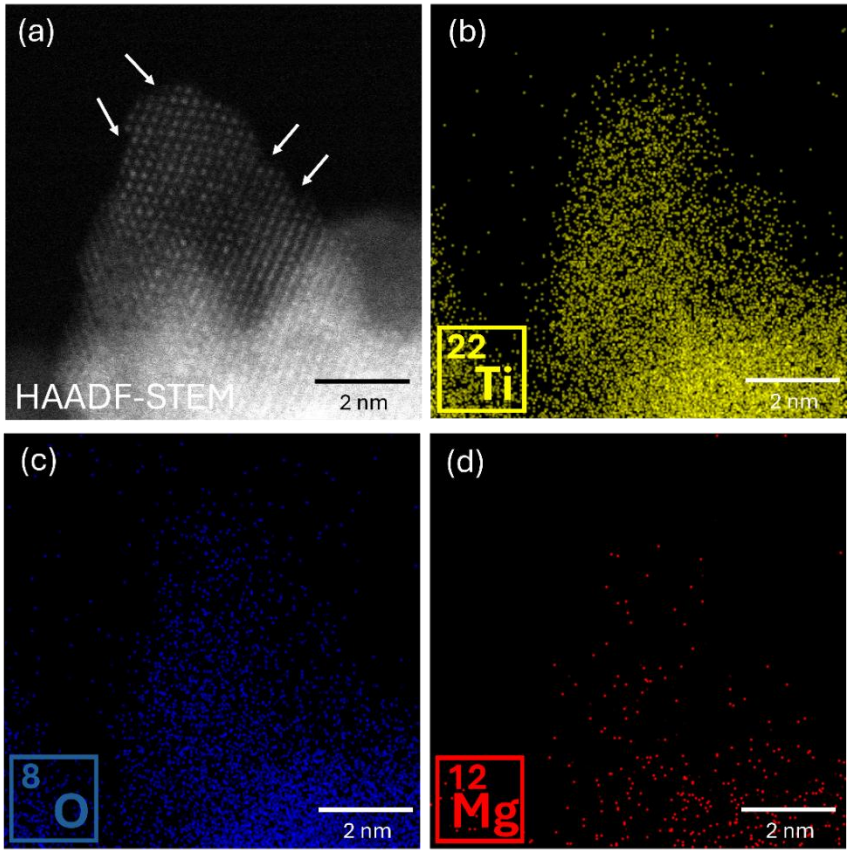

Figure 10: EDS analysis of the 10 mol. % Mg-TiO_2 nanopowder. (a) SE-STEM image and EDS maps of **(b)** Ti, **(c)** O and **(d)** Mg obtained from a single Mg-TiO_2 nanocrystal. The solid arrows point to surface structural defects.

Since a morphology change was observed only for the 10 mol. % Mg-TiO_2 sample, leading to the formation of nanorods (**Figure 8 (d)**) with surface structural defects (**Figure 9 (d)**), which are expected to provide a higher surface area, this composition was selected for further analysis and TE testing [107], [108].

3.1.5 BET Analysis

BET analysis was conducted to determine the specific surface areas of intrinsic TiO_2 and 10 mol. % Mg-TiO_2 NPs. **Figure 11** shows the isotherm curve for intrinsic TiO_2 (**Figure 11 (a)**) and for the 10 mol. % TiO_2-Mg nanomaterials (**Figure 11 (b)**) as well as the corresponding Barrett-Joyner-Halenda (BJH) pore size distribution (**Figure 12 (a) and (b)**) [109-110]. The hysteresis loops observed for both TiO_2 nanopowders corresponded to a type IV isotherm, as classified by International Union of Pure and Applied Chemistry (IUPAC), indicating the presence of a mesoporous TiO_2 (pore size ranging from 2 to 50 nm [109]). The pore size distribution of both nanostructures observed reveal a peak at ≈ 4 nm, indicating that the NPs possess predominantly small mesopores. **Figure 12** further illustrates the uniformity of the pore structure, as evidenced by the sharp and well-defined distribution [110].

The results revealed that Mg incorporation significantly increased the specific surface area (**Table 4**) with values of 141.41 m^2g^{-1} for intrinsic TiO_2 and 256.93 m^2g^{-1} for 10 mol. % Mg-TiO_2. This finding is consistent with the reduction in NPs size observed in **Figure 8 (a) and (d)**, showing average

sizes of 14.54 ± 2.06 nm and 10.60 ± 1.93 nm (**Table 3**), respectively. The inverse relationship between NPs average size and specific surface area is expected and has been widely reported in the literature [111-112]. The extensive presence of surface defects and bulk defects appears to have played a major role in this increase in the specific surface area.

The small pores combined with the increased specific surface area of the 10 mol. % Mg-TiO_2 nanomaterial is anticipated to provide a wider contact surface for cell attachment, thereby enhancing and accelerating the TE process in the periodontium [113-114].

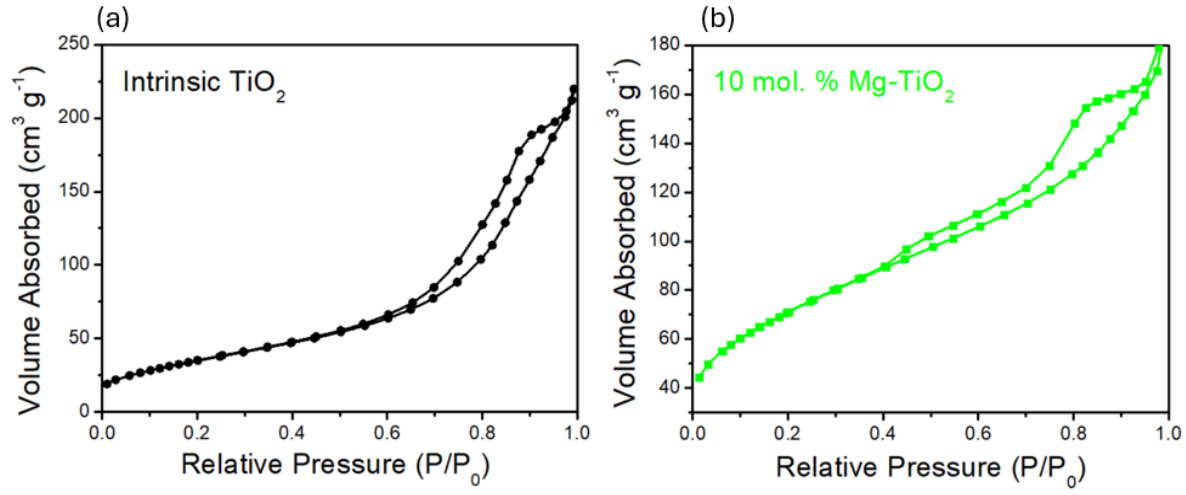

Figure 11: N_2 adsorption-desorption isotherms. (a) Intrinsic TiO_2 and **(b)** 10 mol. % Mg-TiO_2.

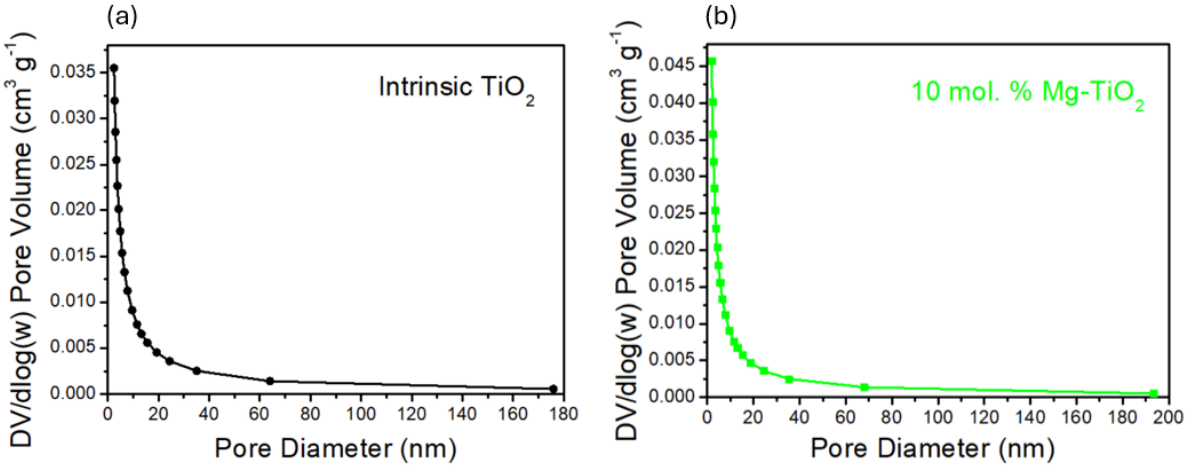

Figure 12: Pore size distribution curves obtained from the BJH analysis of the desorption branches. **(a)** Intrinsic TiO_2 and **(b)** 10 mol. % Mg-TiO_2.

Table 4: Estimated BET specific surface area. Estimated value for the TiO_2 NPs and 10 mol. % Mg-TiO_2.

Specific Surface Area (m^2 g^{-1})	
Intrinsic TiO_2	141.41
10 mol. % Mg-TiO_2	256.93

3.2 Alginate Scaffolds

3.2.1 Morphological Characterization

Morphological characterization was conducted to examine the microstructural features of the composites. The SEM images (**Figure 13**) show surface rugosities in the scaffolds' walls. In the case of the coated scaffolds, the SEM images did not clearly reveal the rough surface structure **(Figure 13 (e) and (f)**), as the surface was covered by a continuous layer formed during the coating process.

The pristine alginate scaffolds (**Figure 13 (a) and (b)**) presented defined irregular and non-spherical superficial rugosities. Variations in surface roughness and pore structure are likely linked to inter-batch variability, a common phenomenon to happen in natural polymers, including alginate [115]. The incorporation of NPs by blending (**Figure 13 (d)**) promoted the formation of more elongated and spherical rugosities, likely due to their interaction with the polymer network and stabilization of pore walls during scaffold formation [116-117]. It's noticeable a partial collapse of the network, which led to a denser and less interconnected structure. Even though the observations were restricted to the surface of the scaffolds, this may reflect differences in internal pore morphology, potentially influencing pore connectivity and spatial distribution [118]. In **Figure 13 (c)** is possible to observe pores in the scaffold via blending which had values that ranged from ≈ 158.45 μm to ≈ 284.14 μm. It has been reported that pores above 100 μm are ideal to promote osteoblast integration [119]. For periodontal TE, values from 150 to 300 μm for the pores' dimensions have been reported [120]. It is important to note that the structures observed in **Figure 13** result from compression of the scaffolds during sectioning, which was performed prior to imaging to obtain a cross-section for analysis. This procedure may, however, compromise the original structural integrity of the scaffolds. Generally, for all the types of scaffolds the rugosities were quite irregular and heterogeneous which reflected in the porous structure. This has already been reported in studies specially when alginate network forms upon crosslinking via external gelation with Ca^{2+} [121].

Moreover, EDS analysis of the pristine alginate scaffolds **(Figure 14 (a), (b)** and **(c)**), the alginate scaffolds containing NPs incorporated via blending (**Figure 14 (d), (e), (f)**, **(g)** and **(h)**) and via coating (**Figure 14 (i), j), (k)**, **(l)** and **(m)**) confirmed the successful integration of the NPs within the scaffold matrix and on the surface, respectively. No additional impurities were detected. The presence of other elements, as shown in **Figure A1** (Appendices), corresponds to the intrinsic composition of the alginate polymer [122].

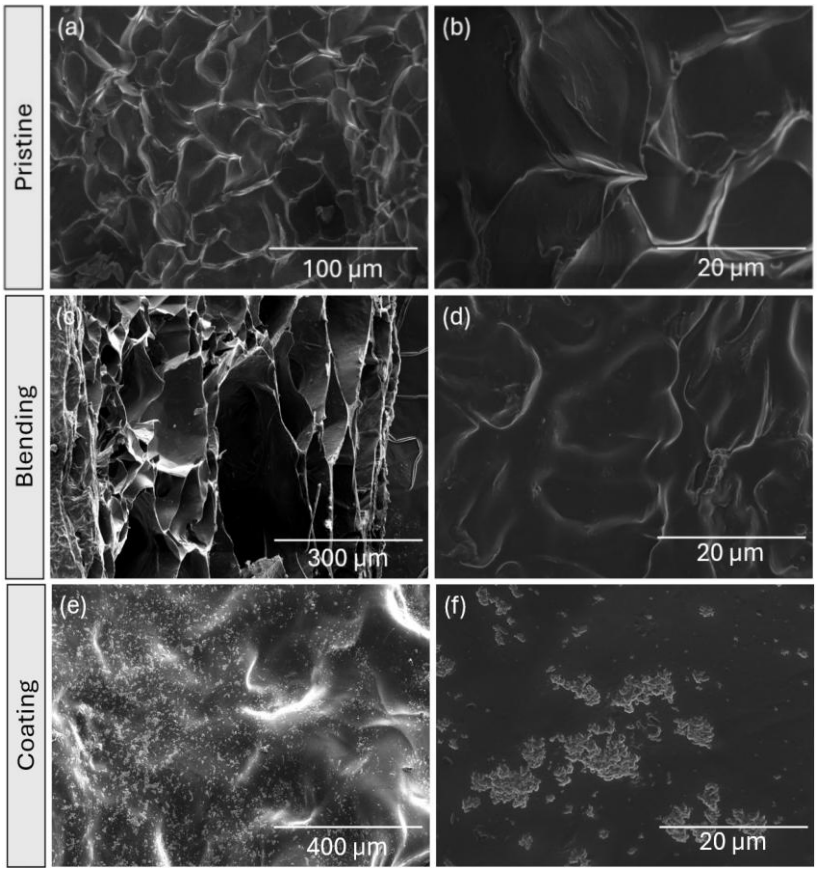

Figure 13: SEM morphological analysis of the scaffolds. (a) and **(b)** pristine alginate scaffold. **(c)** and **(d)** alginate scaffold with NPs incorporated via blending. **(e)** and **(f)** alginate scaffold with NPs incorporated via coating. Scale bares represent 20, 100, 300 and 400 µm as indicated.

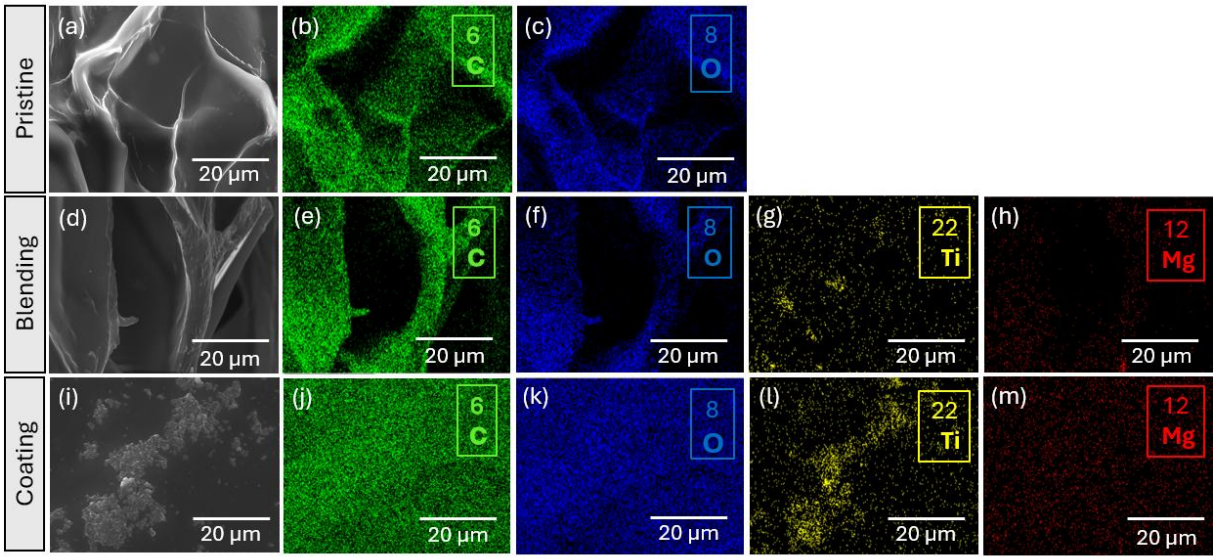

Figure 14: EDS analysis of the alginate scaffolds. (a), **(b)** and **(c)** are pristine alginate scaffolds. **(d)**, **(e)**, **(f)**, **(g)** and **(h)** are alginate scaffolds with NPs incorporated via blending. **(i)**, **(j)**, **(k)** and **(l)** and **(m)** are alginate scaffold with NPs incorporated via coating. **(b)**, **(e)** and **(j)** are maps of C. **(c)**, **(f)** and **(k)** are maps of O. **(g)** and **(l)** are maps of Ti. **(h)** and **(m)** are maps of Mg. Scale bares represent 20 µm as indicated.

3.2.1.1 Porosity of the scaffolds

Scaffold design is critical in TE, providing structural support for tissue formation that mimics *in vivo* conditions [123]. Pore size and porosity are key parameters, as they define the microenvironment and influence mechanical properties, with higher porosity typically reducing strength [124-125]. It's essential to have an interconnected porous network with optimal pore size to ensure effective transport of nutrients, oxygen, and growth factors, while supporting cell attachment and proliferation [125]. To evaluate scaffolds' porosity, **Equation 3** was applied (the dimensions for the calculations are in **Appendix A.1**). As shown in **Figure 15**, the pristine scaffolds exhibited the highest porosity (89.55 ± 0.99 %), followed by the scaffolds prepared via blending (88.38 ± 4.29 %), and then the ones via coating (78.82 ± 2.45 %). Regarding the periodontal tissues, studies mentioned 70 to 86% porosity for adequate bone regeneration [126]. The incorporation via coating had a more pronounced alteration of the porosity compared to the incorporation via blending, aligning closer with the values reported in literature. While porosity is essential for bone tissue scaffolds, facilitating cell infiltration, nutrient transport, and vascularization, excessively high porosity can be harmful to bone regeneration. Extremely porous scaffolds have reduced mechanical strength, which may be insufficient to support physiological loads, leading to structural collapse or deformation *in vivo*.

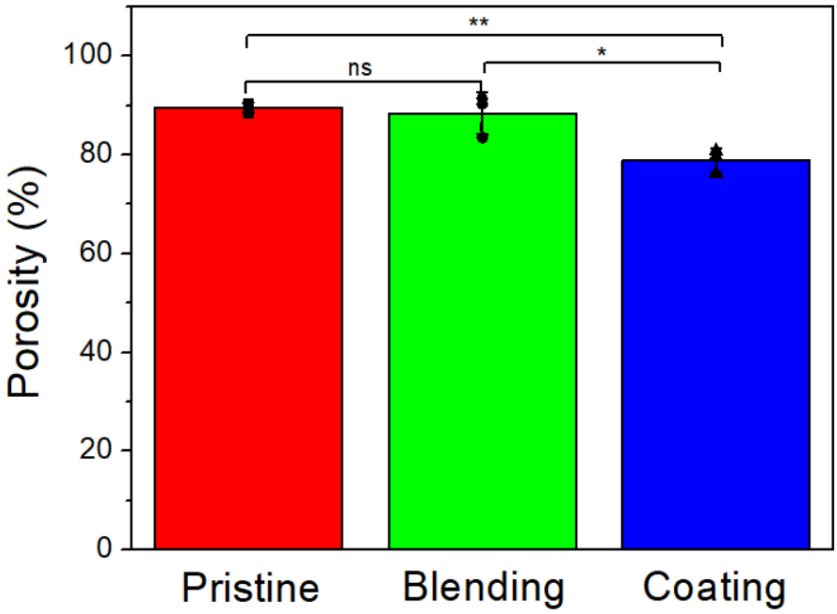

Figure 15: Determination of porosity for the alginate pristine scaffolds and the scaffolds with NPs incorporation by blending and by coating. One-Way ANOVA test, non-significant (ns), *p < 0.05, **p < 0.01. All data presented as plot individual values, mean ± SD (n=3).

3.2.2 Swelling Behaviour

Assessing the swelling capacity of scaffolds is essential, as it directly influences their ability to absorb nutrients and metabolites within the body, which plays a critical role in supporting cell growth and tissue development [127-128]. The water uptake was determined using **Equation 4**.

Consistent with previous reports, the swelling behaviour of alginate scaffolds was strongly influenced by the incorporation of the NPs, as can be observed in **Figure 16** [129-130]. After seven days, the pristine scaffolds exhibited a water uptake of 1458.28 ± 129.87 %, while with the NPs in blending and in coating, 1109.36 ± 182.15 % and 544.26 ± 50.73 %, respectively. Pristine scaffolds exhibited the highest swelling ratio, consistent with the high free volume and chain mobility of the unmodified hydrogel matrix. When NPs were introduced by blending, the swelling ratio decreased. This reduction can be attributed to their function as a filler that occupies free space in the polymeric network [128]. Similar reductions in swelling were also reported by *Zaragoza et al* [131] and *Wu et al* [132] suggesting that NPs have the capacity to act as pseudo crosslinkers and increasing the extent of crosslinking within the alginate network, constraining the relaxation of the polymeric chains and the diffusion of PBS into the scaffold [133]. Scaffolds coated with NPs showed the lowest swelling. In this case, the formation of a surface layer (observable in **Figure 13 (e) and (f)**), likely resulted in a dense barrier that limited water diffusion into the bulk material and restricted ionic exchange processes that normally promote alginate expansion [134-135]. The combined effects of increased crosslinking, reduced porosity and surface diffusion barriers explain the observed hierarchy in swelling behaviour [136].

The swelling rate for all types of scaffolds remained relatively constant over the seven-day period, indicating a gradual and stable water uptake and suggesting that the polymeric network maintains its structural integrity during prolonged hydration [136-137]. A consistent swelling rate ensures uniform delivery of nutrients and metabolites to cells within the scaffold, preserving cellular viability and supporting tissue development. Additionally, it maintains the structural integrity and porosity of the scaffold, which is crucial for cell infiltration and diffusion of bioactive molecules [136-137].

Since excessive water uptake compromises the mechanical integrity of alginate scaffolds, incorporating NPs by blending or coating reinforces the potential of alginate scaffolds for load-bearing applications, particularly relevant for AB regeneration in periodontal tissues [138-139].

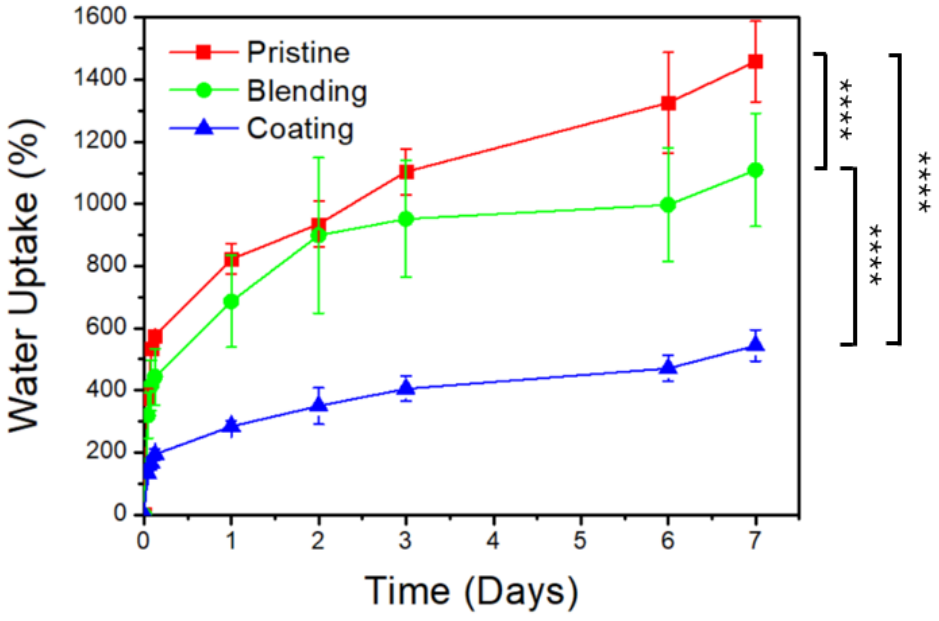

Figure 16: Water Uptake of the alginate scaffolds, pristine, by blending and by coating over a seven-day period. Two-way ANOVA test, ****p < 0.0001. All data presented as plot individual values, mean ± SD (n=3).

3.2.3 Mechanical Essay

The mechanical environment plays an important role in determining scaffold performance once implanted into physiological systems. Scaffolds are continuously exposed to mechanical forces such as compression, tension, shear, and fluid flow, all of which directly influence cellular behaviour [140]. Under cyclic loading, scaffolds inevitably experience fatigue, which can reduce their overall mechanical resistance and long-term stability [141]. At the same time, cyclic mechanical stimuli can act as mechanobiological cues, promoting cellular proliferation and differentiation [140-141].

As shown in **Figure 17**, the Young's Modulus was calculated using **Equation 5**. The incorporation of NPs led to a slight increase in scaffold stiffness, with a Young's Modulus of 0.52 ± 0.34 kPa for scaffolds prepared via blending, and a more pronounced increase to 0.83 ± 0.34 kPa for scaffolds prepared via coating. This trend aligns with the observations in **Figure 15** and **Figure 16**, where coated NPs scaffolds exhibited reduced porosity and lower water uptake, indicating a denser network structure. However, despite the increase, the mechanical reinforcement provided by the NPs was insufficient to reach the Young's Modulus typically required for optimal scaffold performance, contradicting previous reports showing that the incorporation of ceramic NPs into biomaterials generally enhances stiffness that lacks in polymeric scaffolds [120], [142].

In the periodontium, for the AB, an Elastic Modulus of 6.17 x 10^6 kPa has been reported [143]. The incorporation of NPs improved the scaffold's mechanical properties, bringing them closer to *in vivo* conditions. However, the resulting Young's Modulus remained significantly lower than the hard bone tissues in the periodontium. Increasing the NPs content could potentially improve the Elastic Modulus, enabling the scaffold to better approximate the mechanical characteristics of these biological structures.

Despite the limited increase in stiffness, all types of alginate scaffolds demonstrated significant elastic recovery after the compression tests (up to 80% strain), returning almost completely to their original shape once the load was removed, as shown in **Figure A2** (Appendices), proving the shape-memory property of alginate polymers [144-145]. In the periodontal TE context, scaffolds are exposed to cyclic mechanical stresses from chewing and occlusal forces, so this ability ensures that the pore architecture for cell infiltration and nutrient transport is preserved [144].

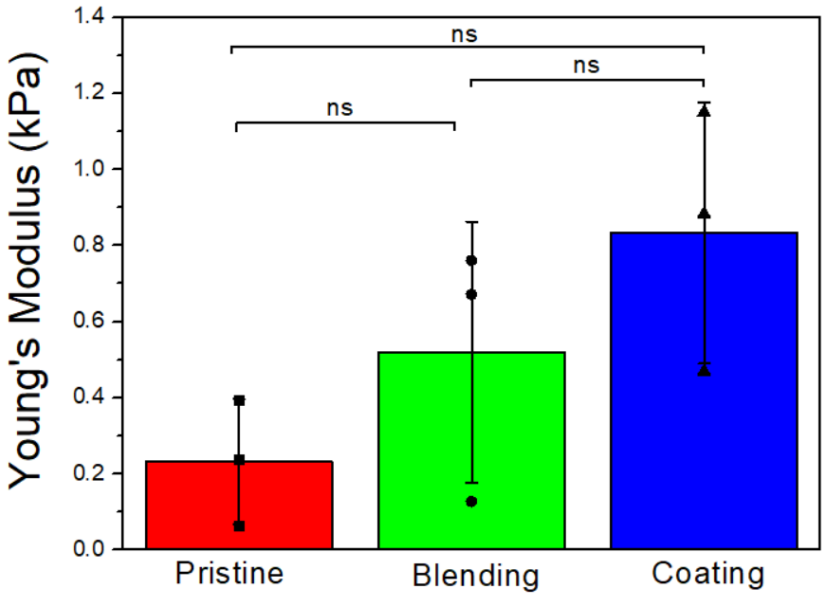

Figure 17: Mechanical characterisation of the alginate pristine scaffolds, by blending and by coating. Determination of the Young's Modulus values for all scaffold types within the initial linear region (20%). One-Way ANOVA test, non-significant (ns). Data presented as plot individual values, mean ± SD (n=3).

3.2.4 Cell Viability (Live/dead Essay)

Cell viability is a widely used and important parameter in TE and culture studies to evaluate the effect of environmental conditions on cell behaviour. Several methods to determinate cell viability on scaffolds have been already studied [146-147]. The live/dead essay using Calcein-AM and PI provides a reliable qualitative and quantitative assessment of cellular responses to different scaffolds compositions [148]. This dual staining technique enables the clear identification of live and dead cells, offering valuable insight into how the scaffolds' composition and surface properties influence cell survival and attachment [148]. Cell viability was determined by **Equation 6**.

The results in **Figure 18** clearly show that the incorporation of the NPs in the scaffold's composition, either by blending or by coating, didn't compromise the cytotoxicity of the alginate scaffolds and showed no significant statistical variation. According to ISO 10993-5, a biomaterial is considered to have cytotoxic potential when cell viability is below 70% [149]. Based on the results presented in **Figure 18**, none of the scaffolds developed in this study exhibited cytotoxic behaviour, even after the incorporation of 10 mol. % Mg-TiO_2 NPs. The pristine scaffolds showed a cell viability of 90.89 ± 1.52 %, while the scaffolds containing NPs incorporated by blending and coating displayed values of 80.64 ± 8.67 % and 71.22 ± 12.15 %, respectively. All remaining above the cytotoxicity threshold. These findings confirm the overall biocompatibility of the scaffolds and are consistent with the literature, as alginate is widely recognized as a non-toxic, biocompatible polymer [23]. TiO_2 NPs have also been extensively reported to exhibit minimal cytotoxicity and good compatibility, supporting their safe integration [43], [59].

These results further corroborated by **Figure 19** clearly demonstrate that the number of viable cells (**Figure 19 (b), (e)** and **(f)**) was markedly higher than that of non-viable cells (**Figure 19 (c)**, **(f)** and **(i)**) across all scaffold types. This indicates that the materials were highly cytocompatible and did

not induce significant cytotoxic effects on Saos-2 cells. The presence of an extensive cyan fluorescence signal and the limited occurrence of magenta spots confirm that most cells maintained membrane integrity and metabolic activity after incubation. These findings support the conclusion that NPs incorporation, either by blending or by coating, did not compromise biocompatibility.

After the live/dead assay it was observed that even though cells remained mainly alive, the incorporation of 10 mol. % Mg-TiO_2 didn't affect the Saos-2-cells adhesion to the scaffolds, which was unexpected. Alginate scaffolds are biologically inert and lack molecular cues for cell recognition and attachment, which contributes to poor cell adhesion [150]. However, numerous studies have shown that incorporating TiO_2 can enhance adhesion by increasing surface roughness and surface energy [151]. The 10 mol. % Mg-TiO_2 NPs exhibited several structural surface defects and a high specific surface area, providing potential anchoring sites for cell attachment [152]. This suggests that the amount of NPs incorporated into the scaffolds may have been insufficient to significantly modify the overall surface topography or chemistry [153]. This is further supported by the observation that the incorporation of NPs did not noticeably improve the mechanical performance of the scaffolds, with stiffness remaining low (**Figure 17**). Although a higher Young's Modulus is typically associated with enhanced cell adhesion, the presence of surface defects and the increased surface area of the 10 mol. % Mg-TiO_2 NPs may have compensated partially for the low stiffness by promoting local interactions between the material and cells [154-155]. These defects can act as active sites for protein adsorption and focal adhesion formation, facilitating cell aggregation and proliferation on the scaffold surface despite the limited mechanical reinforcement [152].

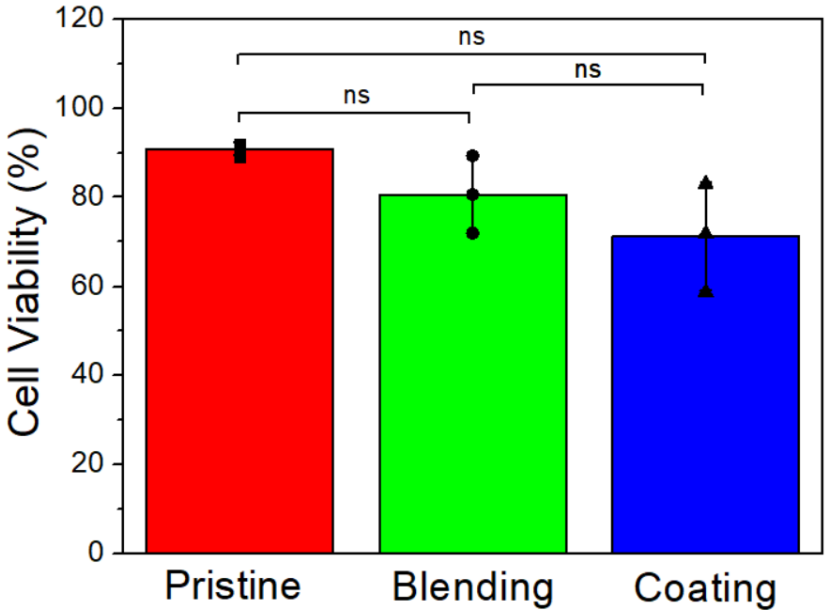

Figure 18: Cell viability of the alginate pristine scaffolds, by blending and by coating. One-Way ANOVA test, non-significant (ns). Data presented as plot individual values, mean ± SD (n=3).

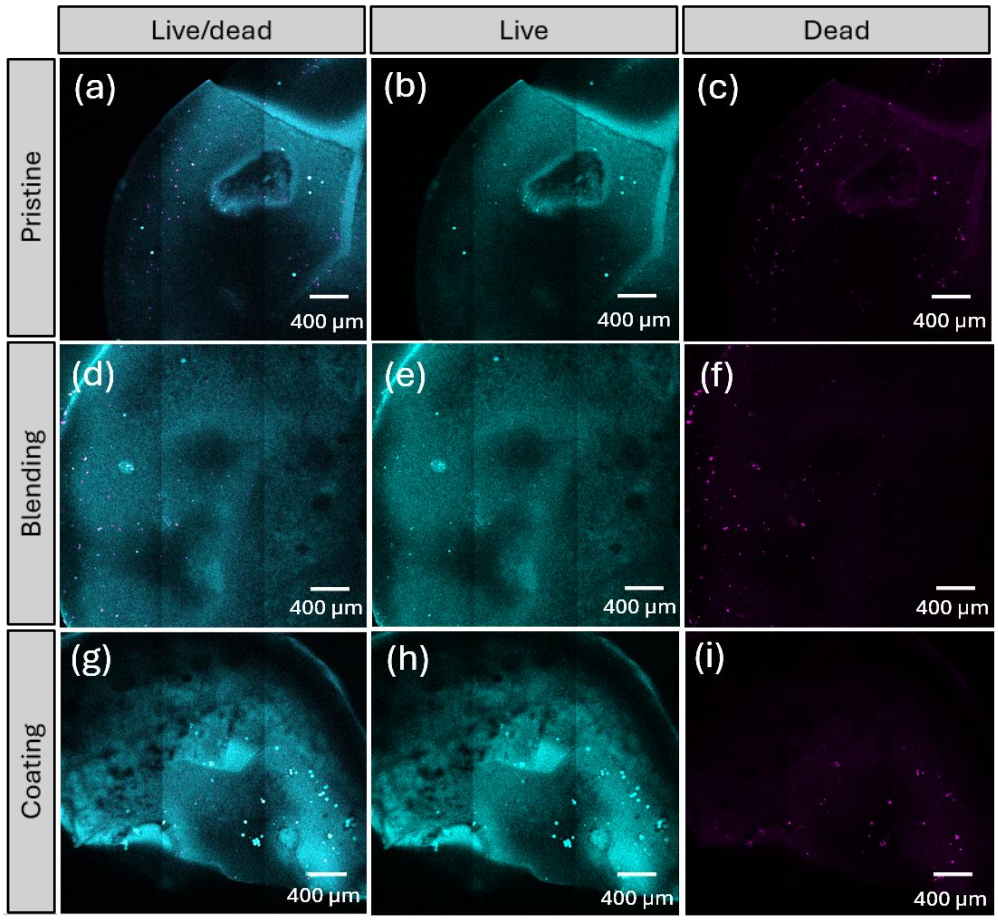

Figure 19: Cell viability imaging. (a), **(d)** and **(g)** are the mixed viable and non-viable cells for the pristine, blending and coating, respectively. **(b)**, **(e)** and **(h)**, are the viable cells for the pristine, blending and coating respectively. **(c)**, **(f)** and **(i)** are the non-viable cells for the pristine, blending and coating respectively.

The results obtained in this study demonstrate that the incorporation of Mg-TiO_2 nanorods into alginate scaffolds maintained good cytocompatibility, showing cell viability above the cytotoxicity threshold defined by ISO 10993-5 [149]. Although the incorporation of NPs did not lead to a significant enhancement in the mechanical performance or in the adhesion of Saos-2 cells, the structural characteristics of the nanorods, namely their elongated morphology, the presence of surface defects, and the increased specific surface area, suggest a potential to promote local interactions between the material and cells. It is likely that the concentration of Mg-TiO_2 NPs used was insufficient to produce marked changes in the alginate scaffolds. Nevertheless, these nanoscale features may have partially compensated for the low stiffness of the composite by facilitating local protein adsorption and initial attachment events. The overall cell mortality remained within acceptable levels, confirming the cytocompatibility of the developed systems. These findings highlight that while the current NPs amount did not significantly improve cell adhesion, the structural and surface characteristics of Mg-TiO_2 nanorods hold promise for further optimization in future TE applications, particularly for periodontal regeneration.

4

CONCLUSION AND FUTURE WORK

The aim of this study was to develop a nanomaterial composed of NPs capable of promoting periodontal tissue regeneration and enhancing the osteoinductive properties of scaffolds. Additionally, a key objective was to achieve this through a sustainable green synthesis approach, minimizing environmental impact while maintaining high material performance.

The Mg-TiO_2 NPs were successfully synthesized using a microwave-assisted hydrothermal approach. A fast, two-step, low-temperature (210 °C) process was employed without any additional heat treatments. Different Mg concentrations (5, 7, and 10 mol. %) were introduced during TiO_2 NPs synthesis. All samples exhibited the anatase crystalline phase, as confirmed by XRD and Raman spectroscopy, with no evidence of rutile, brookite, or Mg-O secondary phases.

UV-Vis analysis was conducted to estimate the Eg of the NPs. The obtained Eg value was approximately 3.10 eV, slightly lower than the typical value reported in the literature for anatase TiO_2. This reduction can be associated with structural defects or oxygen vacancies within the material, confirming the presence of defects in the material.

STEM morphological analysis revealed that increasing Mg content led to a reduction in particle size, from 14.54 ± 2.06 nm for intrinsic TiO_2 to 10.60 ± 1.93 nm for 10 mol. % Mg-TiO_2. The 10 mol. % Mg-TiO_2 sample also exhibited elongated, nanorod-like morphologies. Additionally, 10 mol. % Mg-TiO_2 displayed surface defects and large voids. EDS analysis confirmed the absence of impurities and demonstrated a homogeneous distribution of Ti, O, and Mg elements within the NPs.

BET analysis further emphasized the influence of Mg incorporation, with an increase in specific surface area from 141.41 m^2g^{-1} for intrinsic TiO_2 to 256.93 m^2g^{-1} for 10 mol. % Mg-TiO_2. This finding aligns with the observed reduction in NPs size and the presence of structural defects.

Overall, these results demonstrated that Mg incorporation effectively modified the morphology and surface characteristics of TiO_2 NPs, promoting smaller, defect rich structures with increased surface area.

The 10 mol. % Mg-TiO_2 NPs were incorporated into alginate scaffolds using two distinct approaches: blending and coating. This incorporation via blending noticeably affected the scaffold morphology, resulting in surface rugosities that were less interconnected and defined, with rounder corners. A slight decrease in overall porosity was observed, particularly in the coated samples, which exhibited values more consistent with those reported in the literature (78.82 ± 2.45 %). The addition of NPs also significantly influenced the swelling behaviour, leading to a reduction in water uptake (1109.36 ± 182.15

% for the scaffolds with NPs incorporated via blending and 544.26 ± 50.73 % via coating). Compression assays revealed that scaffolds incorporating NPs via the coating method exhibited the highest Young's modulus (0.83 ± 0.34 kPa), correlating with their reduced porosity and lower water uptake. However, the mechanical differences among all scaffold types were not statistically significant.

The live/dead assay demonstrated that the incorporation of Mg-TiO_2 NPs into the scaffold composition did not significantly affect cytotoxicity, as the differences observed were not statistically significant. The pristine scaffolds showed a cell viability of 90.89 ± 1.52 %, while the scaffolds prepared by blending and coating exhibited 80.64 ± 8.67 % and 71.22 ± 12.15 %, respectively. All values remained well above the cytotoxicity threshold (70 %), confirming the non-toxic nature of the Mg-TiO_2 NPs and their suitability for biomedical applications.

This work demonstrated that a green and sustainable synthesis route can be effectively used to produce Mg-TiO_2 NPs in the anatase phase, taking advantage of the natural abundance and low environmental impact of the constituent elements. When incorporated into alginate scaffolds, these NPs didn't induce cytotoxicity and preserved essential physical characteristics such as porosity and swelling within the ideal ranges described in the literature. Although the current system shows promising biological compatibility, further optimization of the synthesis parameters and scaffold composition may lead to enhanced mechanical properties and improved overall performance for peridontal TE.

4.1 Future work

Despite the lack of literature on Mg-TiO_2 NPs for TE applications, especially in the periodontium, this study proved the potential of this nanomaterial. Although the potential of Mg-TiO_2 NPs for TE applications was shown, several aspects could be further explored to enhance scaffold performance and deepen understanding of the system.

Firstly, further optimization of the green synthesis process should be carried out by exploring a wider range of Mg incorporation levels and refining synthesis parameters such as reaction time, temperature, and microwave power. This would allow a better understanding of how these factors influence NPs size, crystallinity, surface defects, and, ultimately, their biological and mechanical performance.

The optimization of the NPs incorporation within the alginate matrix is essential for enhancing the mechanical properties of the scaffold, particularly its mechanical strength, while maintaining suitable porosity and biocompatibility. Future studies could explore intermediate strategies between blending and coating techniques to improve interfacial bonding and achieve a more uniform NPs distribution throughout the polymer network. Additionally, modifying the crosslinking density of alginate or introducing hybrid reinforcements, such as hydroxyapatite or collagen, may further increase scaffold stiffness and structural stability. It is also important to note that in the present study, the amount of NPs incorporated was relatively low, which may have limited significant changes in the physicochemical composition and mechanical performance of the scaffold. Therefore, higher NPs concentrations or alternative incorporation approaches may be required to observe more pronounced effects.

The extension of the biological evaluation is much needed, including proliferation assays and long-term cytocompatibility under dynamic culture conditions, as well as studies on cell differentiation to further assess the material's potential for TE applications.

Further studies should consider a larger sample size (n) to ensure statistical reliability and reproducibility of the results.

In conclusion, this study highlights the promising potential of Mg-TiO_2 NPs for TE, while also revealing clear opportunities for optimization in synthesis, scaffold design, and biological evaluation. Addressing these aspects could further enhance scaffold performance and reproducibility, paving the way towards more effective and osteoinductive biomaterials.

BIBLIOGRAPHY

[1] P. Mark Bartold, Y. Xiao, S. P. Lyngstaadas, M. L. Paine, and M. L. Snead, "Principles and applications of cell delivery systems for periodontal regeneration." Periodontology 2000, vol. 41, no. 1, pp. 123–135, 2006, doi: 10.1111/j.1600-0757.2006.00156.x

[2] S. Dabra, K. Chhina, N. Soni, and R. Bhatnagar, "Tissue engineering in periodontal regeneration: A brief review," 2012. [Online]. Dental Research Journal (Isfahan), vol. 9, no. 6, pp. 671–680, Nov. 2012, PMID: 23559940, PMCID: PMC3612212

[3] C. Deng, C. Xu, Q. Zhou, and Y. Cheng, "Advances of nanotechnology in osteochondral regeneration," Nov. 01, 2019, *Wiley-Blackwell*. doi: 10.1002/wnan.1576.

[4] H. N. Woo, Y. J. Cho, S. Tarafder, and C. H. Lee, "The recent advances in scaffolds for integrated periodontal regeneration," Oct. 01, 2021, *KeAi Communications Co.* doi: 10.1016/j.bioactmat.2021.03.012.

[5] T. Kwon, I. B. Lamster, and L. Levin, "Current Concepts in the Management of Periodontitis," *Int. Dent. J.*, vol. 71, no. 6, pp. 462–476, Dec. 2021, doi: 10.1111/idj.12630.

[6] X. T. He, R. X. Wu, and F. M. Chen, "Periodontal tissue engineering and regeneration," in *Principles of Tissue Engineering*, Elsevier, 2020, pp. 1221–1249. doi: 10.1016/B978-0-12-818422-6.00068-X.

[7] F. A. Scannapieco and A. Cantos, "Oral inflammation and infection, and chronic medical diseases: implications for the elderly," *Periodontol. 2000.*, vol. 72, no. 1, pp. 153–175, Oct. 2016, doi: 10.1111/prd.12129.

[8] K. F. Al-Shammari, A. K. Al-Khabbaz, J. M. Al-Ansari, R. Neiva, and H. Wang, "Risk Indicators for Tooth Loss Due to Periodontal Disease," *J. Periodontol.*, vol. 76, no. 11, pp. 1910–1918, Nov. 2005, doi: 10.1902/jop.2005.76.11.1910.

[9] F. J. O'Brien, "Biomaterials & scaffolds for tissue engineering," 2011, *Elsevier B.V.* doi: 10.1016/S1369-7021(11)70058-X.

[10] Y. Chen *et al.*, "Mechanical properties and biocompatibility of porous titanium scaffolds for bone tissue engineering," *J. Mech. Behav. Biomed. Mater.*, vol. 75, pp. 169–174, Nov. 2017, doi: 10.1016/j.jmbbm.2017.07.015.

[11] D. Yang, J. Xiao, B. Wang, L. Li, X. Kong, and J. Liao, "The immune reaction and degradation fate of scaffold in cartilage/bone tissue engineering," *Materials Science and Engineering: C*, vol. 104, p. 109927, Nov. 2019, doi: 10.1016/j.msec.2019.109927.

[12] B. P. Chan and K. W. Leong, "Scaffolding in tissue engineering: General approaches and tissue-specific considerations," in *European Spine Journal*, Dec. 2008. doi: 10.1007/s00586-008-0745-3.

[13] M. Krishani, W. Y. Shin, H. Suhaimi, and N. S. Sambudi, "Development of Scaffolds from Bio-Based Natural Materials for Tissue Regeneration Applications: A Review," *Gels*, vol. 9, no. 2, p. 100, Jan. 2023, doi: 10.3390/gels9020100.

[14] S. Swain, P. Swain, S. K. Parida, and T. R. Rautray, "Ceramic scaffolds for biomaterials applications," in *Advanced Ceramic Coatings for Biomedical Applications*, Elsevier, 2023, pp. 223–248. doi: 10.1016/B978-0-323-99626-6.00016-0.

[15] Y. Ikada, "Challenges in tissue engineering," Oct. 22, 2006, *Royal Society*. doi: 10.1098/rsif.2006.0124.

[16] S. Safinsha and M. Mubarak Ali, "Composite scaffolds in tissue engineering," *Mater. Today Proc.*, vol. 24, pp. 2318–2329, 2020, doi: 10.1016/j.matpr.2020.03.761.

[17] L. Lu *et al.*, "In vitro and in vivo degradation of porous poly(dl-lactic-co-glycolic acid) foams," *Biomaterials*, vol. 21, no. 18, pp. 1837–1845, Sep. 2000, doi: 10.1016/S0142-9612(00)00047-8.

[18] N. Farshidfar, S. Iravani, and R. S. Varma, "Alginate-Based Biomaterials in Tissue Engineering and Regenerative Medicine," *Mar. Drugs*, vol. 21, no. 3, p. 189, Mar. 2023, doi: 10.3390/md21030189.

[19] J. Zhu *et al.*, "Advanced application of collagen-based biomaterials in tissue repair and restoration," Dec. 01, 2022, *Springer*. doi: 10.1186/s42825-022-00102-6.

[20] A. Hasan, M. Morshed, A. Memic, S. Hassan, T. J. Webster, and H. E. S. Marei, "Nanoparticles in tissue engineering: Applications, challenges and prospects," 2018, *Dove Medical Press Ltd.* doi: 10.2147/IJN.S153758.

[21] J. Danie Kingsley, S. Ranjan, N. Dasgupta, and P. Saha, "Nanotechnology for tissue engineering: Need, techniques and applications," *J. Pharm. Res.*, vol. 7, no. 2, pp. 200–204, Feb. 2013, doi: 10.1016/j.jopr.2013.02.021.

[22] R. Abka-khajouei, L. Tounsi, N. Shahabi, A. K. Patel, S. Abdelkafi, and P. Michaud, "Structures, Properties and Applications of Alginates," *Mar. Drugs*, vol. 20, no. 6, p. 364, May 2022, doi: 10.3390/md20060364.

[23] S. L. Tomić, M. M. Babić Radić, J. S. Vuković, V. V. Filipović, J. Nikodinovic-Runic, and M. Vukomanović, "Alginate-Based Hydrogels and Scaffolds for Biomedical Applications," Mar. 01, 2023, *Multidisciplinary Digital Publishing Institute (MDPI)*. doi: 10.3390/md21030177.

[24] K. Y. Lee and D. J. Mooney, "Alginate: Properties and biomedical applications," 2012, *Elsevier Ltd*. doi: 10.1016/j.progpolymsci.2011.06.003.

[25] O. Guillaume, A. Daly, K. Lennon, J. Gansau, S. F. Buckley, and C. T. Buckley, "Shape-memory porous alginate scaffolds for regeneration of the annulus fibrosus: Effect of TGF-β3 supplementation and oxygen culture conditions," *Acta Biomater.*, vol. 10, no. 5, pp. 1985–1995, 2014, doi: 10.1016/j.actbio.2013.12.037.

[26] S. Heiligenstein *et al.*, "*In Vitro* and *In Vivo* Characterization of Nonbiomedical- and Biomedical-Grade Alginates for Articular Chondrocyte Transplantation," *Tissue Eng. Part C Methods*, vol. 17, no. 8, pp. 829–842, Aug. 2011, doi: 10.1089/ten.tec.2010.0681.

[27] J. Qin, F. Chen, P. Wu, and G. Sun, "Recent Advances in Bioengineered Scaffolds for Cutaneous Wound Healing," *Front. Bioeng. Biotechnol.*, vol. 10, Mar. 2022, doi: 10.3389/fbioe.2022.841583.

[28] C. C. Piras, C. S. Mahon, and D. K. Smith, "Self-Assembled Supramolecular Hybrid Hydrogel Beads Loaded with Silver Nanoparticles for Antimicrobial Applications," *Chemistry – A European Journal*, vol. 26, no. 38, pp. 8452–8457, Jul. 2020, doi: 10.1002/chem.202001349.

[29] T. Duruel, A. S. Çakmak, A. Akman, R. M. Nohutcu, and M. Gümüşderelioğlu, "Sequential IGF-1 and BMP-6 releasing chitosan/alginate/PLGA hybrid scaffolds for periodontal regeneration," *Int. J. Biol. Macromol.*, vol. 104, pp. 232–241, Nov. 2017, doi: 10.1016/j.ijbiomac.2017.06.029.

[30] Z. Ye, W. Xu, R. Shen, and Y. Yan, "Emulsion electrospun PLA/calcium alginate nanofibers for periodontal tissue engineering," *J. Biomater. Appl.*, vol. 34, no. 6, pp. 763–777, Jan. 2020, doi: 10.1177/0885328219873561.

[31] S. Srinivasan, R. Jayasree, K. P. Chennazhi, S. V. Nair, and R. Jayakumar, "Biocompatible alginate/nano bioactive glass ceramic composite scaffolds for periodontal tissue regeneration," *Carbohydr. Polym.*, vol. 87, no. 1, pp. 274–283, Jan. 2012, doi: 10.1016/j.carbpol.2011.07.058.

[32] H. V. Almeida, B. N. Sathy, I. Dudurych, C. T. Buckley, F. J. O'Brien, and D. J. Kelly, "Anisotropic Shape-Memory Alginate Scaffolds Functionalized with Either Type I or Type II Collagen for Cartilage Tissue Engineering," *Tissue Eng. Part A*, vol. 23, no. 1–2, pp. 55–68, Jan. 2017, doi: 10.1089/ten.TEA.2016.0055.

[33] M. Yadid, R. Feiner, and T. Dvir, "Gold Nanoparticle-Integrated Scaffolds for Tissue Engineering and Regenerative Medicine," *Nano Lett.*, vol. 19, no. 4, pp. 2198–2206, Apr. 2019, doi: 10.1021/acs.nanolett.9b00472.

[34] S. Chowdhury and S. Chakraborty, "Gold nanoparticles in tissue engineering," in *Nanostructured Materials for Tissue Engineering*, Elsevier, 2023, pp. 399–423. doi: 10.1016/B978-0-323-95134-0.00011-0.

[35] A. Damle, R. Sundaresan, J. M. Rajwade, P. Srivastava, and A. Naik, “A concise review on implications of silver nanoparticles in bone tissue engineering,” *Biomaterials Advances*, vol. 141, p. 213099, Oct. 2022, doi: 10.1016/j.bioadv.2022.213099.

[36] M. Godoy-Gallardo *et al.*, “Antibacterial approaches in tissue engineering using metal ions and nanoparticles: From mechanisms to applications,” *Bioact. Mater.*, vol. 6, no. 12, pp. 4470–4490, Dec. 2021, doi: 10.1016/j.bioactmat.2021.04.033.

[37] D. D. Chakraborty, S. Pramanik, and P. Chakraborty, “Quantum dots in tissue engineering,” in *Nanostructured Materials for Tissue Engineering*, Elsevier, 2023, pp. 385–397. doi: 10.1016/B978-0-323-95134-0.00010-9.

[38] L. Bao, X. Cui, M. Mortimer, X. Wang, J. Wu, and C. Chen, “The renaissance of one-dimensional carbon nanotubes in tissue engineering,” *Nano Today*, vol. 49, p. 101784, Apr. 2023, doi: 10.1016/j.nantod.2023.101784.

[39] V. Goranov, “Biomaterials functionalized with magnetic nanoparticles for tissue engineering: Between advantages and challenges,” *Biomaterials and Biosystems*, vol. 15, p. 100100, Sep. 2024, doi: 10.1016/j.bbiosy.2024.100100.

[40] R. Sensenig, Y. Sapir, C. MacDonald, S. Cohen, and B. Polyak, “Magnetic nanoparticle-based approaches to locally target therapy and enhance tissue regeneration in vivo,” Sep. 2012. doi: 10.2217/nnm.12.109.

[41] M. Fathi-Achachelouei *et al.*, “Use of Nanoparticles in Tissue Engineering and Regenerative Medicine,” *Front. Bioeng. Biotechnol.*, vol. 7, May 2019, doi: 10.3389/fbioe.2019.00113.

[42] S. M. Gupta and M. Tripathi, “A review of TiO2 nanoparticles,” Jun. 2011. doi: 10.1007/s11434-011-4476-1.

[43] C. Y. Hsu *et al.*, “Nano titanium oxide (nano-TiO2): A review of synthesis methods, properties, and applications,” *Case Studies in Chemical and Environmental Engineering,* vol. 9, Art. no. 100626, 2024, doi: 10.1016/j.cscee.2024.100626.

[44] G. Žerjav, K. Žižek, J. Zavašnik, and A. Pintar, “Brookite vs. rutile vs. anatase: What`s behind their various photocatalytic activities.” *J. Environ. Chem. Eng.*, vol. 10, no. 3, p. 107722, Jun. 2022, doi: 10.1016/j.jece.2022.107722.

[45] D. A. H. Hanaor and C. C. Sorrell, “Review of the anatase to rutile phase transformation,” *J. Mater. Sci.*, vol. 46, no. 4, pp. 855–874, Feb. 2011, doi: 10.1007/s10853-010-5113-0.

[46] L. Lv, K. Li, Y. Xie, Y. Cao, and X. Zheng, “Enhanced osteogenic activity of anatase TiO 2 film: Surface hydroxyl groups induce conformational changes in fibronectin,” *Materials Science and Engineering: C*, vol. 78, pp. 96–104, Sep. 2017, doi: 10.1016/j.msec.2017.04.056.

[47] J. Zhang *et al.*, “Nanotexture and crystal phase regulation for synergistic enhancement in re-endothelialization on medical pure titanium surface,” *Mater. Today Bio*, vol. 25, p. 100968, Apr. 2024, doi: 10.1016/j.mtbio.2024.100968.

[48] H. Nosrati and M. Heydari, “Titanium dioxide nanoparticles: a promising candidate for wound healing applications,” *Burns Trauma*, vol. 13, 2025, doi: 10.1093/burnst/tkae069.

[49] B. Kolathupalayam Shanmugam, S. Rangaraj, K. Subramani, S. Srinivasan, W. K. Aicher, and R. Venkatachalam, "Biomimetic TiO2-chitosan/sodium alginate blended nanocomposite scaffolds for tissue engineering applications," *Materials Science and Engineering C*, vol. 110, May 2020, doi: 10.1016/j.msec.2020.110710.

[50] P. Kumar, "Nano-TiO2 Doped Chitosan Scaffold for the Bone Tissue Engineering Applications," *International Journal of Biomaterials,* vol. 2018, Art. no. 6576157, pp. 1–7, 2018, doi: 10.1155/2018/6576157.

[51] M. Dhayal *et al.*, "Strategies to prepare TiO2 thin films, doped with transition metal ions, that exhibit specific physicochemical properties to support osteoblast cell adhesion and proliferation," *Materials Science and Engineering: C*, vol. 37, pp. 99–107, Apr. 2014, doi: 10.1016/j.msec.2013.12.035.

[52] A. Saberi, M. S. Baltatu, and P. Vizureanu, "Recent Advances in Magnesium–Magnesium Oxide Nanoparticle Composites for Biomedical Applications," May 01, 2024, *Multidisciplinary Digital Publishing Institute (MDPI)*. doi: 10.3390/bioengineering11050508.

[53] I. Antoniac *et al.*, "Additive Manufactured Magnesium-Based Scaffolds for Tissue Engineering," *Materials*, vol. 15, no. 23, p. 8693, Dec. 2022, doi: 10.3390/ma15238693.

[54] M. Yazdimamaghani, M. Razavi, D. Vashaee, K. Moharamzadeh, A. R. Boccaccini, and L. Tayebi, "Porous magnesium-based scaffolds for tissue engineering," *Materials Science and Engineering: C*, vol. 71, pp. 1253–1266, Feb. 2017, doi: 10.1016/j.msec.2016.11.027.

[55] K. Athira, K. T. Merin, T. Raguram, and K. S. Rajni, "Synthesis and characterization of Mg doped TiO2 nanoparticles for photocatalytic applications," *Mater. Today Proc.*, vol. 33, pp. 2321–2327, 2020, doi: 10.1016/j.matpr.2020.04.580.

[56] X. Zheng, P. Zhang, Z. Fu, S. Meng, L. Dai, and H. Yang, "Applications of nanomaterials in tissue engineering," May 13, 2021, *Royal Society of Chemistry*. doi: 10.1039/d1ra01849c.

[57] R. U. K. Shenoy, A. Rama, I. Govindan, and A. Naha, "The purview of doped nanoparticles: Insights into their biomedical applications," Nov. 01, 2022, *Elsevier Inc.* doi: 10.1016/j.onano.2022.100070.

[58] B. Li and Y. Jin, "Periodontal Tissue Engineering," in *Stem Cell Biology and Tissue Engineering in Dental Sciences*, Elsevier, 2015, pp. 471–482. doi: 10.1016/B978-0-12-397157-9.00041-2.

[59] Q. Junnan, L. Huimin, L. Guihong, and C. Yao, "Innovation of TiO2-x Nanomaterials in the Biomedical Field: Synthesis, Properties, and Application Prospects," *Chemical Engineering Journal*, vol. 491, p. 151773, Jul. 2024, doi: 10.1016/j.cej.2024.151773.

[60] Z. Du *et al.*, "Calcium silicate scaffolds promoting bone regeneration via the doping of Mg2+ or Mn2+ ion," *Compos. B Eng.*, vol. 190, p. 107937, Jun. 2020, doi: 10.1016/j.compositesb.2020.107937.

[61] Z. Shan, X. Xie, X. Wu, S. Zhuang, and C. Zhang, "Development of degradable magnesium-based metal implants and their function in promoting bone metabolism (A review)," *J. Orthop. Translat.*, vol. 36, pp. 184–193, Sep. 2022, doi: 10.1016/j.jot.2022.09.013.

[62] M. S. Samuel *et al.*, "A Review on Green Synthesis of Nanoparticles and Their Diverse Biomedical and Environmental Applications," *Catalysts*, vol. 12, no. 5, p. 459, Apr. 2022, doi: 10.3390/catal12050459.

[63] A. K. Kar *et al.*, "Comparative study on green versus chemical synthesis for metallic NPs with respect to physicochemical characterization and toxicity," *Next Materials*, vol. 9, p. 101184, Oct. 2025, doi: 10.1016/j.nxmate.2025.101184.

[64] A. Kumar, Y. Kuang, Z. Liang, and X. Sun, "Microwave chemistry, recent advancements, and eco-friendly microwave-assisted synthesis of nanoarchitectures and their applications: a review," *Mater. Today Nano*, vol. 11, p. 100076, Aug. 2020, doi: 10.1016/j.mtnano.2020.100076.

[65] M. L. Matias *et al.*, "Functionalized 3D polyurethane foams with microwave-synthesized TiO 2 nanostructures for solar light-driven degradation of tetracycline," *Environmental Science: Advances*, vol. 4, no. 5, pp. 713–738, 2025, doi: 10.1039/D4VA00110A.

[66] A. Ahmad *et al.*, "Role of XRD for nanomaterial analysis," in *Nanomedicine Manufacturing and Applications*, Elsevier, 2021, pp. 149–161. doi: 10.1016/B978-0-12-820773-4.00008-1.

[67] P. Makuła, M. Pacia, and W. Macyk, "How To Correctly Determine the Band Gap Energy of Modified Semiconductor Photocatalysts Based on UV–Vis Spectra," *J. Phys. Chem. Lett.*, vol. 9, no. 23, pp. 6814–6817, Dec. 2018, doi: 10.1021/acs.jpclett.8b02892.

[68] H. Moradi, A. Eshaghi, S. R. Hosseini, and K. Ghani, "Fabrication of Fe-doped TiO2 nanoparticles and investigation of photocatalytic decolorization of reactive red 198 under visible light irradiation," *Ultrason. Sonochem.*, vol. 32, pp. 314–319, Sep. 2016, doi: 10.1016/j.ultsonch.2016.03.025.

[69] J. Zhang, W. Liu, P. Wang, and K. Qian, "Photocatalytic behavior of cellulose-based paper with TiO2 loaded on carbon fibers," *J. Environ. Chem. Eng.*, vol. 1, no. 3, pp. 175–182, Sep. 2013, doi: 10.1016/j.jece.2013.04.022.

[70] P. Yadav, G. Beniwal, and K. K. Saxena, "A review on pore and porosity in tissue engineering," in *Materials Today: Proceedings*, Elsevier Ltd, 2021, pp. 2623–2628. doi: 10.1016/j.matpr.2020.12.661.

[71] I. Rubio-Elizalde *et al.*, "Scaffolds based on alginate-PEG methyl ether methacrylate-Moringa oleifera-Aloe vera for wound healing applications," *Carbohydr. Polym.*, vol. 206, pp. 455–467, Feb. 2019, doi: 10.1016/j.carbpol.2018.11.027.

[72] B. V. Arévalo-Jaimes and E. Torrents, "Died or Not Dyed: Assessment of Viability and Vitality Dyes on Planktonic Cells and Biofilms from Candida parapsilosis," *Journal of Fungi*, vol. 10, no. 3, Mar. 2024, doi: 10.3390/jof10030209.

[73] M. L. Matias *et al.*, "Enhanced Fe-TiO2 Solar Photocatalysts on Porous Platforms for Water Purification," *Nanomaterials*, vol. 12, no. 6, Art. no. 1005, 2022, doi: 10.3390/nano12061005.

[74] A. P, K. T, D. S, J. J, A. F. Abd El-Rehim, and E. R. Kumar, "Evaluation of structural, optical and morphological properties of La doped TiO2 nanoparticles," *Ceram. Int.*, vol. 49, no. 11, pp. 16991–16998, Jun. 2023, doi: 10.1016/j.ceramint.2023.02.061.

[75] G. Raja *et al.*, "Effect of lattice strain on structure, morphology, electrical conductivity and magneto-optical and catalytic properties of Ni-doped Mn3O4 nano-crystallites synthesized by microwave route," *Journal of Saudi Chemical Society*, vol. 26, no. 2, Mar. 2022, doi: 10.1016/j.jscs.2022.101440.

[76] S. Dolabella, A. Borzì, A. Dommann, and A. Neels, "Lattice Strain and Defects Analysis in Nanostructured Semiconductor Materials and Devices by High-Resolution X-Ray Diffraction: Theoretical and Practical Aspects," Feb. 01, 2022, *John Wiley and Sons Inc*. doi: 10.1002/smtd.202100932.

[77] F. Yang, W. Luo, J. Wang, and L. Xiang, "Effects of Mg2+ doped TiO2 defect structures on TiO2 anatase-to-rutile phase transition," *J. Alloys Compd.*, vol. 958, p. 170529, Oct. 2023, doi: 10.1016/j.jallcom.2023.170529.

[78] M. L. Matias *et al.*, "Defect-Engineered Ca-TiO2 Nanomaterials for Enhanced Adsorption and Photocatalytic Degradation of Water Pollutants on Sustainable Cellulose Membranes," *Advanced Sustainable Systems,* vol. 9, no. 10, 2025, doi: 10.1002/adsu.202500675.

[79] S. Bharatbhai Akhani, J. Pathak, T. Akhani, and M. Singh Rathore, "Structural and optical properties of Mg doped TiO2 nanoparticles synthesized by sol-gel method," *Mater. Today Proc.*, Feb. 2024, doi: 10.1016/j.matpr.2024.02.029.

[80] M. Fazil, S. M. Alshehri, Y. Mao, and T. Ahmad, "Hydrothermally Derived Mg-Doped TiO2 Nanostructures for Enhanced H2 Evolution Using Photo- and Electro-Catalytic Water Splitting," *Catalysts*, vol. 13, no. 5, p. 893, May 2023, doi: 10.3390/catal13050893.

[81] S. Challagulla, K. Tarafder, R. Ganesan, and S. Roy, "Structure sensitive photocatalytic reduction of nitroarenes over TiO2," *Sci. Rep.*, vol. 7, no. 1, Dec. 2017, doi: 10.1038/s41598-017-08599-2.

[82] J. Zhang, M. Li, Z. Feng, J. Chen, and C. Li, "UV raman spectroscopic study on TiO2- I. phase transformation at the surface and in the bulk," *The Journal of Physical Chemistry B,* vol. 110, no. 2, pp. 927–935, 2005, doi: 10.1021/jp0552473.

[83] N. S. Portillo-Vélez, O. Olvera-Neria, I. Hernández-Pérez, and A. Rubio-Ponce, "Localized electronic states induced by oxygen vacancies on anatase TiO2 (101) surface," *Surf. Sci.*, vol. 616, pp. 115–119, Oct. 2013, doi: 10.1016/j.susc.2013.06.006.

[84] Y.-H. Lu, K. Chang, and Y.-F. Chen, "Electronic Structure Modulation from Configuring Anatase TiO2 into a Bicontinuous Mesostructure."

[85] S. Guan *et al.*, "Oxygen vacancies induced band gap narrowing for efficient visible-light response in carbon-doped TiO2," *Sci. Rep.*, vol. 13, no. 1, p. 14105, Aug. 2023, doi: 10.1038/s41598-023-39523-6.

[86] B. Choudhury and A. Choudhury, "Defect generation, d-d transition, and band gap reduction in Cu-doped TiO 2 nanoparticles," *International Nano Letters,* vol. 3, no. 1, Art. no. 25, 2013, doi: 10.1186/2228-5326-3-25.

[87] O. Adedokun, P. Sivaprakash, A. S. Ajani, I. T. Bello, and S. Arumugam, "Structural, optical and magnetic studies of sol-gel synthesized Mg-doped pure anatase TiO2 nanoparticles for

spintronic and optoelectronics applications," *International Nano Letters,* vol. 3, no. 1, Art. no. 25, 2013, doi: 10.1186/2228-5326-3-25.

[88] P. R. Jubu, F. K. Yam, V. M. Igba, and K. P. Beh, "Tauc-plot scale and extrapolation effect on bandgap estimation from UV–vis–NIR data – A case study of β-Ga2O3," *J. Solid State Chem.*, vol. 290, p. 121576, Oct. 2020, doi: 10.1016/j.jssc.2020.121576.

[89] S. Lin, F. Yang, Z. Yang, J. Wang, and L. Xiang, "Preparation of Hydrated TiO2 Particles by Hydrothermal Hydrolysis of Mg/Al-Bearing TiOSO4 Solution," *Nanomaterials,* vol. 13, no. 7, Art. no. 1179, 2023, doi: 10.3390/nano13071179.

[90] S. Jaybhaye, N. Shinde, S. Jaybhaye, and H. Narayan, "Photocatalytic Degradation of Organic Dyes Using Titanium Dioxide (TiO 2) and Mg-TiO 2 Nanoparticles," 2022.

[91] B. Padmaja, S. Dhanapandian, and K. Ashokkumar, "Hydrothermally derived Mg doped tin oxide nanostructures for photocatalytic and supercapacitor applications," *Materials Science and Engineering: B*, vol. 297, p. 116699, Nov. 2023, doi: 10.1016/j.mseb.2023.116699.

[92] B. Cojocaru, D. Avram, V. Kessler, V. Parvulescu, G. Seisenbaeva, and C. Tiseanu, "Nanoscale insights into doping behavior, particle size and surface effects in trivalent metal doped," *Sci. Rep.*, vol. 7, no. 1, Dec. 2017, doi: 10.1038/s41598-017-09026-2.

[93] M. Taeño, D. Maestre, J. Ramírez-Castellanos, S. Li, P. S. Lee, and A. Cremades, "Towards Control of the Size, Composition and Surface Area of NiO Nanostructures by Sn Doping," *Nanomaterials*, vol. 11, no. 2, p. 444, Feb. 2021, doi: 10.3390/nano11020444.

[94] K. Manseki, T. Ikeya, A. Tamura, T. Ban, T. Sugiura, and T. Yoshida, "Mg-doped TiO 2 nanorods improving open-circuit voltages of ammonium lead halide perovskite solar cells," *RSC Adv.*, vol. 4, no. 19, pp. 9652–9655, 2014, doi: 10.1039/C3RA47870J.

[95] K. Erdogar, O. Yucel, and M. E. Oruc, "Investigation of Structural, Morphological, and Optical Properties of Novel Electrospun Mg-Doped TiO2 Nanofibers as an Electron Transport Material for Perovskite Solar Cells," *Nanomaterials*, vol. 13, no. 15, p. 2255, Aug. 2023, doi: 10.3390/nano13152255.

[96] K. Santhi, M. Navaneethan, S. Harish, S. Ponnusamy, and C. Muthamizhchelvan, "Synthesis and characterization of TiO2 nanorods by hydrothermal method with different pH conditions and their photocatalytic activity," *Appl. Surf. Sci.*, vol. 500, p. 144058, Jan. 2020, doi: 10.1016/j.apsusc.2019.144058.

[97] S. Cai, C. Wu, W. Yang, W. Liang, H. Yu, and L. Liu, "Recent advance in surface modification for regulating cell adhesion and behaviors," *Nanotechnol. Rev.*, vol. 9, no. 1, pp. 971–989, Jan. 2020, doi: 10.1515/ntrev-2020-0076.

[98] Y. H. Ahmad, A. S. Abu Hatab, A. T. Mohamed, M. S. Al-Kuwari, A. S. Aljaber, and S. Y. Al-Qaradawi, "Microwave-Assisted Solvothermal Synthesis of Mo-Doped TiO2 with Exceptional Textural Properties and Superior Adsorption Kinetics," *Nanomaterials*, vol. 12, no. 12, p. 2051, Jun. 2022, doi: 10.3390/nano12122051.

[99] J. Flores Cantera, J. A. Wang, S. P. Paredes Carrea, L. F. Chen, J. Salmones, and J. González, "A microwave-ultrasound assisted synthesis of defective TiO2 and WO3/TiO2 nanoparticles for

ultralow sulfur diesel production," *Mater. Lett.*, vol. 360, p. 136030, Apr. 2024, doi: 10.1016/j.matlet.2024.136030.

[100] Y.-J. Zhu and F. Chen, "Microwave-Assisted Preparation of Inorganic Nanostructures in Liquid Phase," *Chem. Rev.*, vol. 114, no. 12, pp. 6462–6555, Jun. 2014, doi: 10.1021/cr400366s.

[101] D. Briševac, I. Gabelica, D. Ljubas, A. Bafti, G. Matijašić, and L. Ćurković, "Effects of TiO2 Nanoparticles Synthesized via Microwave Assistance on Adsorption and Photocatalytic Degradation of Ciprofloxacin," *Molecules*, vol. 29, no. 12, p. 2935, Jun. 2024, doi: 10.3390/molecules29122935.

[102] Y. Sun, Z. Zhang, J. Yang, X. Wang, H. Peng, and J. Peng, "Microwave-assisted synthesis of oxygen vacancy associated Bi–TiO 2 nanocomposite for degradation of rhodamine B under visible light irradiation," *React. Chem. Eng.*, vol. 9, no. 6, pp. 1521–1531, 2024, doi: 10.1039/D3RE00644A.

[103] R. Thundiyil, P. Poornesh, K. Ozga, and J. Jedryka, "An insight in to microwave induced defects and its impact on nonlinear process in NiO nanostructures under femtosecond and continuous wave laser excitation," *RSC Adv.*, vol. 14, no. 41, pp. 30011–30036, 2024, doi: 10.1039/D4RA06056C.

[104] W. Ahmad, S. Kumar, and S. Ahmed, "Microwave-assisted one-step biosynthesis of titanium dioxide nanoparticles: Antibacterial, antioxidant, and photocatalytic properties," *Kuwait Journal of Science*, vol. 51, no. 2, p. 100203, Apr. 2024, doi: 10.1016/j.kjs.2024.100203.

[105] M. Catauro, E. Tranquillo, G. Dal Poggetto, M. Pasquali, A. Dell'Era, and S. Vecchio Ciprioti, "Influence of the Heat Treatment on the Particles Size and on the Crystalline Phase of TiO2 Synthesized by the Sol-Gel Method," *Materials*, vol. 11, no. 12, p. 2364, Nov. 2018, doi: 10.3390/ma11122364.

[106] S. Rachmaniar, D. A. Nugraha, D. J. D. H. Santjojo, R. T. Tjahjanto, N. Mufti, and Masruroh, "Prevention of particle agglomeration in sol–gel synthesis of TiO2 nanoparticles via addition of surfactant," *Journal of Nanoparticle Research*, vol. 26, no. 3, p. 45, Mar. 2024, doi: 10.1007/s11051-024-05943-2.

[107] S. D. Yuan *et al.*, "Obtaining Ultra-High Surface Area TiO2 Nanorods via Hydrothermally Transformation of Elongated Titanate Nanotubes," *Journal of Nano Research,* vol. 51, pp. 13–23, 2018, doi: 10.4028/www.scientific.net/JNanoR.51.13.

[108] Y. Zhang and J. Yan, "Recent advances in the synthesis of defective TiO2 nanofibers and their applications in energy and catalysis," *Chemical Engineering Journal*, vol. 472, Art. no. 144831, 2023, doi: 10.1016/j.cej.2023.144831.

[109] S. Y. Ryu, D. S. Kim, J. D. Jeon, and S. Y. Kwak, "Pore size distribution analysis of mesoporous TiO2 spheres by 1H nuclear magnetic resonance (NMR) cryoporometry," *Journal of Physical Chemistry C*, vol. 114, no. 41, pp. 17440–17445, Oct. 2010, doi: 10.1021/jp105496h.

[110] G. He, J. Zhang, Y. Hu, Z. Bai, and C. Wei, "Dual-template synthesis of mesoporous TiO2 nanotubes with structure-enhanced functional photocatalytic performance," *Appl. Catal. B*, vol. 250, pp. 301–312, Aug. 2019, doi: 10.1016/j.apcatb.2019.03.027.

[111] Peter. Birkle and I. S. . Torres-Alvarado, “Correlation between particle size and surface area for chlorite and K-feldspar”, in *Water-Rock Interaction – Proceedings of the 13th International Conference on Water-Rock Interaction (WRI-13)*, London, UK: Taylor & Francis/CRC Press, 2010, pp. 717–720, ISBN: 978-0-415-60426-0.

[112] M. Sagawa, S. Yamashita, and Y. Okada, “A more accurate estimation of the specific surface area of TiO 2 nanoparticles capped with organic ligands,” *Nanoscale Adv.*, vol. 7, no. 17, pp. 5161–5165, 2025, doi: 10.1039/D5NA00732A.

[113] K. Cai *et al.*, “Effects of titanium nanoparticles on adhesion, migration, proliferation, and differentiation of mesenchymal stem cells,” *Int. J. Nanomedicine*, p. 3619, Sep. 2013, doi: 10.2147/IJN.S38992.

[114] J. V. Calazans Neto, M. L. da C. Valente, and A. C. dos Reis, “Effect of pores on cell adhesion to additively manufactured titanium implants: A systematic review,” *J. Prosthet. Dent.*, vol. 133, no. 4, pp. 990–997, Apr. 2025, doi: 10.1016/j.prosdent.2023.05.010.

[115] I. M. Adel, M. F. ElMeligy, and N. A. Elkasabgy, “Conventional and Recent Trends of Scaffolds Fabrication: A Superior Mode for Tissue Engineering,” *Pharmaceutics*, vol. 14, no. 2, p. 306, Jan. 2022, doi: 10.3390/pharmaceutics14020306.

[116] Z. Zhang *et al.*, “Nanoparticle-Reinforced Hydrogel with a Well-Defined Pore Structure for Sustainable Drug Release and Effective Wound Healing,” *ACS Appl. Bio Mater.*, vol. 8, no. 2, pp. 1406–1417, Feb. 2025, doi: 10.1021/acsabm.4c01659.

[117] A. Kakapour *et al.*, “An Injectable IPN Nanocomposite Hydrogel Embedding Nano Silica for Tissue Engineering Application,” *Macromol. Mater. Eng.*, vol. 310, no. 1, Jan. 2025, doi: 10.1002/mame.202400242.

[118] H. Lee, S.-H. Ahn, and G. H. Kim, “Three-Dimensional Collagen/Alginate Hybrid Scaffolds Functionalized with a Drug Delivery System (DDS) for Bone Tissue Regeneration,” *Chemistry of Materials*, vol. 24, no. 5, pp. 881–891, Mar. 2012, doi: 10.1021/cm200733s.

[119] S. Yamahara *et al.*, “Appropriate pore size for bone formation potential of porous collagen type I-based recombinant peptide,” *Regen. Ther.*, vol. 21, pp. 294–306, Dec. 2022, doi: 10.1016/j.reth.2022.08.001.

[120] T. Luo, B. Tan, L. Zhu, Y. Wang, and J. Liao, “A Review on the Design of Hydrogels With Different Stiffness and Their Effects on Tissue Repair,” *Front. Bioeng. Biotechnol.*, vol. 10, Jan. 2022, doi: 10.3389/fbioe.2022.817391.

[121] J. Girón-Hernández, P. Gentile, and M. Benlloch-Tinoco, “Impact of heterogeneously cross-linked calcium alginate networks on the encapsulation of β-carotene-loaded beads,” *Carbohydr. Polym.*, vol. 271, p. 118429, Nov. 2021, doi: 10.1016/j.carbpol.2021.118429.

[122] P. Shahbazi, M. Abdouss, M. Naeimi, G. Darbemamieh, and M. Jafari-Nodoushan, “Synthesis, fabrication and characterization of composite scaffolds employing sodium alginate, nanoclay and hydroxyapatite for articular cartilage tissue engineering,” *Carbohydrate Polymer Technologies and Applications*, vol. 10, p. 100771, Jun. 2025, doi: 10.1016/j.carpta.2025.100771.

[123] R. Yang *et al.*, "In vitro and in vivo evaluation of hydrogel-based scaffold for bone tissue engineering application," *Arabian Journal of Chemistry*, vol. 16, no. 7, p. 104799, Jul. 2023, doi: 10.1016/j.arabjc.2023.104799.

[124] T. Ramdhan, S. H. Ching, S. Prakash, and B. Bhandari, "Physical and mechanical properties of alginate based composite gels," *Trends Food Sci. Technol.*, vol. 106, pp. 150–159, Dec. 2020, doi: 10.1016/j.tifs.2020.10.002.

[125] F. Mukasheva, L. Adilova, A. Dyussenbinov, B. Yernaimanova, M. Abilev, and D. Akilbekova, "Optimizing scaffold pore size for tissue engineering: insights across various tissue types," *Front. Bioeng. Biotechnol.*, vol. 12, Nov. 2024, doi: 10.3389/fbioe.2024.1444986.

[126] M. Soleimani *et al.*, "Optimization and fabrication of alginate scaffold for alveolar bone regeneration with sufficient drug release," *Int. Nano Lett.*, vol. 11, no. 3, pp. 295–305, Sep. 2021, doi: 10.1007/s40089-021-00342-0.

[127] W. Feng and Z. Wang, "Tailoring the Swelling-Shrinkable Behavior of Hydrogels for Biomedical Applications," *Advanced Science*, vol. 10, no. 28, Oct. 2023, doi: 10.1002/advs.202303326.

[128] M. M. Babić Radić, M. Vukomanović, J. Nikodinović-Runić, and S. Tomić, "Gelatin-/Alginate-Based Hydrogel Scaffolds Reinforced with TiO2 Nanoparticles for Simultaneous Release of Allantoin, Caffeic Acid, and Quercetin as Multi-Target Wound Therapy Platform," *Pharmaceutics*, vol. 16, no. 3, Mar. 2024, doi: 10.3390/pharmaceutics16030372.

[129] M. Ghanbari, M. Salavati-Niasari, and F. Mohandes, "Nanocomposite scaffolds based on gelatin and alginate reinforced by Zn2SiO4 with enhanced mechanical and chemical properties for tissue engineering," *Arabian Journal of Chemistry*, vol. 15, no. 4, p. 103730, Apr. 2022, doi: 10.1016/j.arabjc.2022.103730.

[130] M. Ghanbari, M. Salavati-Niasari, F. Mohandes, Z. Firouzi, and S.-D. Mousavi, "The impact of zirconium oxide nanoparticles content on alginate dialdehyde-gelatin scaffolds in cartilage tissue engineering," *J. Mol. Liq.*, vol. 335, p. 116531, Aug. 2021, doi: 10.1016/j.molliq.2021.116531.

[131] J. Zaragoza *et al.*, "Experimental Investigation of Mechanical and Thermal Properties of Silica Nanoparticle-Reinforced Poly(acrylamide) Nanocomposite Hydrogels," *PLoS One*, vol. 10, no. 8, p. e0136293, Aug. 2015, doi: 10.1371/journal.pone.0136293.

[132] L. Wu, L. Zeng, H. Chen, and C. Zhang, "Effects of silica sol content on the properties of poly(acrylamide)/silica composite hydrogel," *Polymer Bulletin*, vol. 68, no. 2, pp. 309–316, Jan. 2012, doi: 10.1007/s00289-011-0536-6.

[133] A. Chang, N. Babhadiashar, E. Barrett-Catton, and P. Asuri, "Role of nanoparticle-polymer interactions on the development of double-network hydrogel nanocomposites with high mechanical strength," *Polymers (Basel).*, vol. 12, no. 2, Feb. 2020, doi: 10.3390/polym12020470.

[134] M. U. A. Khan *et al.*, "Synthesis of silver-coated bioactive nanocomposite scaffolds based on grafted beta-glucan/hydroxyapatite via freeze-drying method: Anti-microbial and biocompatibility evaluation for bone tissue engineering," *Materials*, vol. 13, no. 4, Feb. 2020, doi: 10.3390/ma13040971.

[135] P. Kesharwani, A. Bisht, A. Alexander, V. Dave, and S. Sharma, "Biomedical applications of hydrogels in drug delivery system: An update," *J. Drug Deliv. Sci. Technol.*, vol. 66, p. 102914, Dec. 2021, doi: 10.1016/j.jddst.2021.102914.

[136] S. M. Bittner *et al.*, "Swelling Behaviors of 3D Printed Hydrogel and Hydrogel-Microcarrier Composite Scaffolds," *Tissue Eng. Part A*, vol. 27, no. 11–12, pp. 665–678, Jun. 2021, doi: 10.1089/ten.tea.2020.0377.

[137] K. Zhang, W. Feng, and C. Jin, "Protocol efficiently measuring the swelling rate of hydrogels," *MethodsX*, vol. 7, p. 100779, 2020, doi: 10.1016/j.mex.2019.100779.

[138] M. Kessler, T. Yuan, J. M. Kolinski, and E. Amstad, "Influence of the Degree of Swelling on the Stiffness and Toughness of Microgel-Reinforced Hydrogels," *Macromol. Rapid Commun.*, vol. 44, no. 16, Aug. 2023, doi: 10.1002/marc.202200864.

[139] G. Funda *et al.*, "Nanotechnology Scaffolds for Alveolar Bone Regeneration," *Materials*, vol. 13, no. 1, p. 201, Jan. 2020, doi: 10.3390/ma13010201.

[140] A. M. Kloxin, C. J. Kloxin, C. N. Bowman, and K. S. Anseth, "Mechanical Properties of Cellularly Responsive Hydrogels and Their Experimental Determination," *Advanced Materials*, vol. 22, no. 31, pp. 3484–3494, Aug. 2010, doi: 10.1002/adma.200904179.

[141] S. S. Lee, X. Du, I. Kim, and S. J. Ferguson, "Scaffolds for bone-tissue engineering," Sep. 07, 2022, *Cell Press*. doi: 10.1016/j.matt.2022.06.003.

[142] A. K. Gaharwar, N. A. Peppas, and A. Khademhosseini, "Nanocomposite hydrogels for biomedical applications," *Biotechnol. Bioeng.*, vol. 111, no. 3, pp. 441–453, Mar. 2014, doi: 10.1002/bit.25160.

[143] M. C. Chang *et al.*, "Elasticity of alveolar bone near dental implant–bone interfaces after one month's healing," *J. Biomech.*, vol. 36, no. 8, pp. 1209–1214, Aug. 2003, doi: 10.1016/S0021-9290(03)00113-1.

[144] M. R. Pfau and M. A. Grunlan, "Smart scaffolds: shape memory polymers (SMPs) in tissue engineering," *J. Mater. Chem. B*, vol. 9, no. 21, pp. 4287–4297, 2021, doi: 10.1039/D1TB00607J.

[145] X. He *et al.*, "Shape memory composite hydrogel based on sodium alginate dual crosslinked network with carboxymethyl cellulose," *Eur. Polym. J.*, vol. 156, p. 110592, Aug. 2021, doi: 10.1016/j.eurpolymj.2021.110592.

[146] R. Dittmar, E. Potier, M. Van Zandvoort, and K. Ito, "Assessment of cell viability in three-dimensional scaffolds using cellular auto-fluorescence," *Tissue Eng. Part C Methods*, vol. 18, no. 3, pp. 198–204, Mar. 2012, doi: 10.1089/ten.tec.2011.0334.

[147] B. Gantenbein-Ritter, E. Potier, S. Zeiter, M. van der Werf, C. M. Sprecher, and K. Ito, "Accuracy of Three Techniques to Determine Cell Viability in 3D Tissues or Scaffolds," *Tissue Eng. Part C Methods*, vol. 14, no. 4, pp. 353–358, Dec. 2008, doi: 10.1089/ten.tec.2008.0313.

[148] S. Lambrecht, A. Gazizova, S. Kara, J. Meyer, and S. Jopp, "Antimicrobial properties and biocompatibility of semi-synthetic carbohydrate-based ionic hydrogels," *RSC Adv.*, vol. 14, no. 42, pp. 30719–30731, 2024, doi: 10.1039/D4RA05695G.

[149] I. Kovrlija *et al.*, “Challenging applicability of ISO 10993-5 for calcium phosphate biomaterials evaluation: Towards more accurate in vitro cytotoxicity assessment,” *Biomaterials Advances*, vol. 160, p. 213866, Jun. 2024, doi: 10.1016/j.bioadv.2024.213866.

[150] B. Zumbo, B. Guagnini, B. Medagli, D. Porrelli, and G. Turco, “Fibronectin Functionalization: A Way to Enhance Dynamic Cell Culture on Alginate/Hydroxyapatite Scaffolds,” *J. Funct. Biomater.*, vol. 15, no. 8, Aug. 2024, doi: 10.3390/jfb15080222.

[151] R. R. Koshy *et al.*, “Tissue Engineering Scaffold Material with Enhanced Cell Adhesion and Angiogenesis from Soy Protein Isolate Loaded with Bio Modulated Micro-TiO 2 Prepared via Prolonged Sonication for Wound Healing Applications,” *ACS Biomater. Sci. Eng.*, vol. 8, no. 11, pp. 4896–4908, Nov. 2022, doi: 10.1021/acsbiomaterials.2c00548.

[152] B. Majhy, P. Priyadarshini, and A. K. Sen, “Effect of surface energy and roughness on cell adhesion and growth – facile surface modification for enhanced cell culture,” *RSC Adv.*, vol. 11, no. 25, pp. 15467–15476, 2021, doi: 10.1039/D1RA02402G.

[153] K. B. Narayanan, “Nanotopographical Features of Polymeric Nanocomposite Scaffolds for Tissue Engineering and Regenerative Medicine: A Review,” May 01, 2025, *Multidisciplinary Digital Publishing Institute (MDPI)*. doi: 10.3390/biomimetics10050317.

[154] M. I. Neves, L. Moroni, and C. C. Barrias, “Modulating Alginate Hydrogels for Improved Biological Performance as Cellular 3D Microenvironments,” Jun. 30, 2020, *Frontiers Media S.A.* doi: 10.3389/fbioe.2020.00665.

[155] Z. Zhang *et al.*, “Impact Analysis of Microscopic Defect Types on the Macroscopic Crack Propagation in Sintered Silver Nanoparticles,” *Computer Modeling in Engineering & Sciences*, vol. 139, no. 1, pp. 441–458, 2024, doi: 10.32604/cmes.2023.043616.

A

APPENDICES

A.1 Scaffolds Measurements

Measurements of the mass and dimensions of the scaffolds were performed using a balance and a digital micrometer to determine their densities (ρ), which were required for calculating the porosity of the structures (**Figure 15**). The experimental results obtained from 3 replicates (n=3) of each scaffold type are presented below in **Tables A1**, **A2** and **A3**.

Table A1: Pristine scaffolds' mass and dimensions for porosity calculations (n=3).

	n = 1	**n = 2**	**n = 3**
w (g)	0.0076	0.0071	0.0068
Height (mm)	1.7570	1.1810	1.7490
Diameter (mm)	2.9040	3.0100	3.1430
Volume (mm^3)	11.6400	8.3800	13.5600
ρ (g/mm^3)	0.0007	0.0008	0.0005

Table A2: Blending incorporation scaffolds' mass and dimensions for porosity calculations (n=3).

	n = 1	**n = 2**	**n = 3**
w (g)	0.0093	0.0089	0.0083
Height (mm)	1.6270	1.6055	1.5260
Diameter (mm)	2.7490	2.6805	2.4650
Volume (mm^3)	9.6400	9.0700	7.2600
ρ (g/mm^3)	0.0010	0.0010	0.0011

Table A3: Coating incorporation scaffolds' mass and dimensions for porosity calculations (n=3).

	n = 1	**n = 2**	**n = 3**
w (g)	0.0133	0.0144	0.0159
Height (mm)	1.1910	1.0015	1.8565
Diameter (mm)	2.1700	2.2520	1.8565
Volume (mm^3)	4.4000	3.9900	5.0200
ρ (g/mm^3)	0.0030	0.0036	0.0032

A.2 EDS mapping of the scaffolds

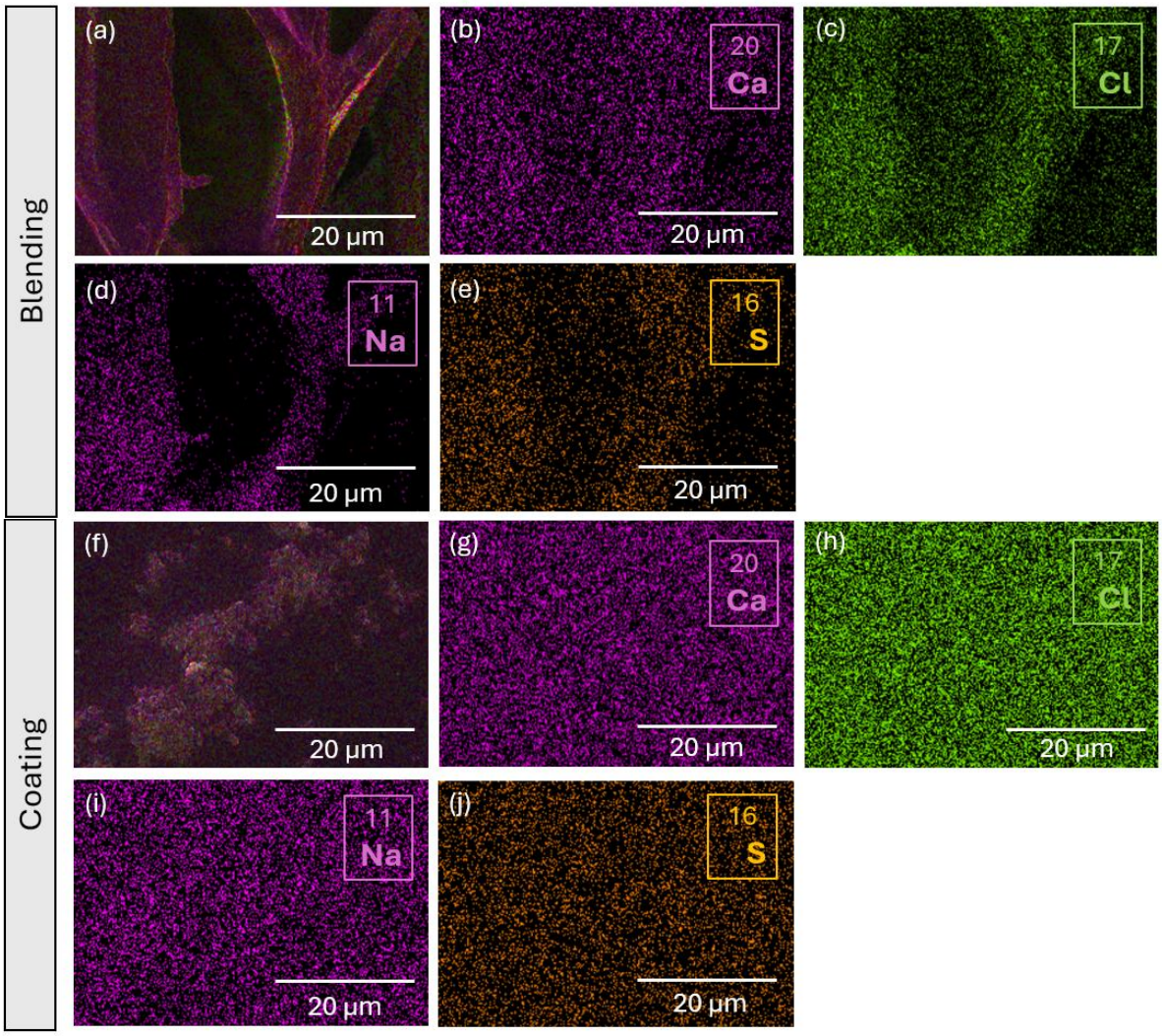

Figure A1: EDS analysis of all types of scaffolds. (a) and **(F)** are the mix EDS maps, **(b)** and **(g)** are the maps for calcium, **(c)** and **(h)** are the maps for chlorine, **(d)** and **(i)** are the maps for sodium and **(e)** and **(j)** are the maps for sulfur.

EDS analyses for the scaffolds incorporated with NPs via blending and via coating are represented in **Figure A1**, with color mapping of the elements present in the samples. All elements detected in the structures correspond to those originating from the reagents and materials used during scaffold fabrication, with no evidence of impurities or foreign elements in any sample.

A.3 Compression Essay

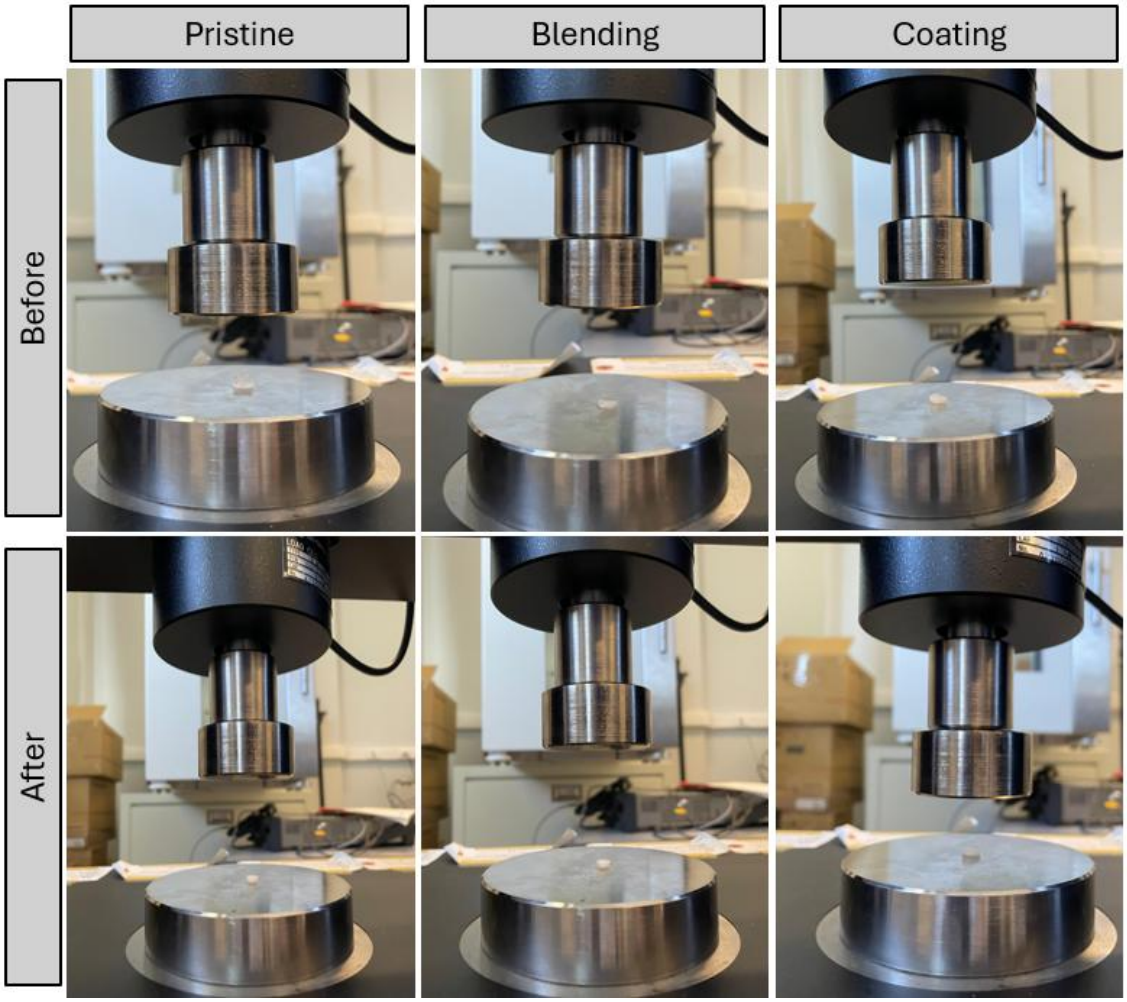

Figure A2: Images of the compression essay. No deformation of the scaffolds observed, proving their shape-memory property.

After the compression test, all scaffold samples: pristine, blending, and coating, fully recovered their original shape, as shown in **Figure A2**. This behaviour confirms the presence of shape-memory properties in the alginate-based scaffolds, allowing them to regain their initial dimensions after the applied compressive load was released. The reversible deformation demonstrates the material's structural integrity and resilience, which are advantageous features for handling and implantation in TE applications, especially in periodontal TE, where scaffolds are subjected to continuous cyclic mechanical forces generated during mastication for example, requiring materials capable of maintaining their structural integrity and functionality overtime.

A.4 All types of scaffolds

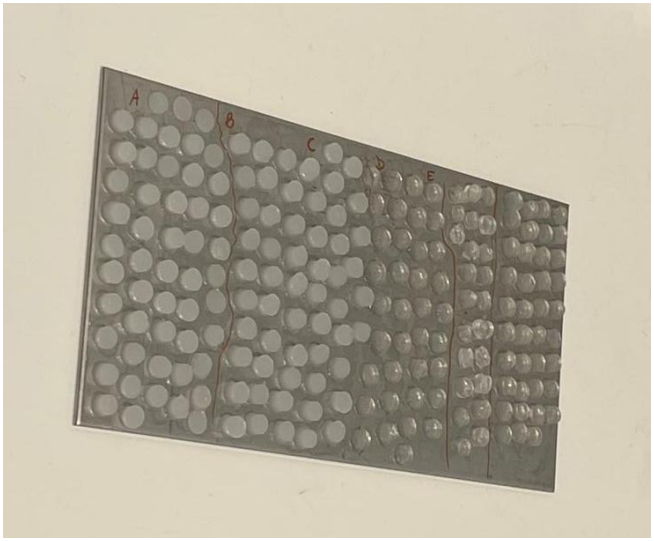

Figure A3: A, B and C show the scaffolds with NPs incorporated by blending. D and E show the scaffolds incorporated by coating. F show the pristine scaffolds.